Radio Frequency and Terahertz Plasmons in Two Dimensional Electron Gases

Citation
Chee, Jingyee. 2018. Radio Frequency and Terahertz Plasmons in Two Dimensional Electron Gases. Doctoral dissertation, Harvard University, Graduate School of Arts & Sciences.

Permanent link
http://nrs.harvard.edu/urn-3:HUL.InstRepos:41126856

Terms of Use

Share Your Story

RADIO FREQUENCY AND TERAHERTZ PLASMONS IN TWO
DIMENSIONAL ELECTRON GASES

A dissertation presented
by
JING YEE CHEE
to
The Harvard John A. Paulson School of
Engineering and Applied Science

in partial fulfillment of the requirements
for the degree of
Doctor of Philosophy
in the subject of

APPLIED PHYSICS

Harvard University
Cambridge, Massachusetts

March 2018

Thesis Advisor
Donhee Ham

Author
Jing Yee Chee

RADIO FREQUENCY AND TERAHERTZ PLASMONS IN TWO

DIMENSIONAL ELECTRON GASES

ABSTRACT

At the turn of the 21st century, the study of photonics, plasmonics and subwavelength phenomena became more and more intense as it became apparent that innovations in these fields could have important and widespread applications in miniaturizing electronic or photonic devices. Recent work in the Ham group have shown that the microwave to far infrared plasmons of 2D electron gases can achieve very small propagation velocities of $< c/100$, enabled by large kinetic inductances of the 2D electron gases, which promises size reduction factors of microwave circuits of 100 times or more.

We will first build and describe simple circuit models of 2D electron gas plasmons, by computing equivalent capacitance, inductance, and resistances. Building a transmission line model from these circuit elements allows us to calculate plasmonic wave dispersions. Modifications to the dispersions are studied, and in particular, we examine how a periodic geometry can result in a plasmonic crystal. We propose and demonstrate these far infrared plasmonic crystals using the 2D electron gas in graphene, and we show that concepts from photonic and electronic crystals such as band engineering and symmetry selection rules apply.

We also examine in great detail the origin and form of the kinetic inductance, which is key to the plasmonic response, and calculate the modifications to the Johnson-Nyquist noise that must necessarily result from any conductor with intrinsic inductance. An understanding of the high frequency noise spectrum is necessary to evaluate potential microwave and far infrared devices using these plasmons.

Lastly, we show how non-reciprocal plasmons can arise non-magnetically, by simply applying a drift current to the electrons. The plasmons carried along by the electrons also drift with the same velocity as the drift velocity, which modifies the plasmon dispersion non-reciprocally, due to the drift motion being non-reciprocal. This principle may enable novel devices based on this principle in the future.

Contents

Acknowledgements

A great many people have helped in me in the course of my PhD studies, and it is my wish to acknowledge their contribution and express my utmost gratitude to each of them.

First and foremost, I would thank my dissertation advisor, Prof. Donhee Ham, without whom this project would not have been possible. He enabled me to have the freedom to pursue my own research interests, and provided guidance when I could not see the right paths. He trained me in how to present my work confidently and articulately, both in writing and in more informal settings. He relentlessly and tirelessly worked to ensure that all the diverse research in our group could be funded, putting the needs of all the students (and post-docs) first. I could not have asked for a more capable and patient advisor.

I also have to thank my colleagues, especially Hosang Yoon and Kitty Yeung who taught me how to overcome the difficulties of RF experiments and worked with me to help produce my first publications here. The other students and postdocs working on 2D materials, Liu Chengye, Wu Jundong, David Rakhmilevitch, and Houk Jang have all provided invaluable help and advice. All the other members of the Ham group have also contributed in some way or another to this work. Jeffrey Abbott, especially, was always an inspiration and could always assist whenever I needed help in concepts that I was unfamiliar with.

List of Tables

List of Figures

Chapter 1

Introduction

Plasmons are oscillations of the local electron density $n(\mathbf{x})$ of an electron gas. The study of such plasma oscillations have led to a better understanding of a rich and diverse multitude of physical phenomena, ranging from the reflectivity and dielectric constant of metals, radio wave guiding by the ionosphere to astrophysical phenomena. In the most technical sense, plasmons are the quantum quasiparticle associated with these plasma oscillations, but as we shall see in the systems we can access experimentally, quantum interference effects from plasmons will not easily be observed, and so we shall use the term plasmon to describe the classical excitation of arbitrarily small amplitude. In this introductory chapter we will attempt to provide an overview of the behaviour of plasmons both from a pedagogical point of view, and as a background for most of the work in this thesis.

1.1 Metal plasmonics in 3D

As an example system, we will begin with the semi-classical Sommerfeld model of a metal. In this model, the ions are fixed, and only the valence electrons of a metal are free within the surface boundary of the metal, which serve as a quantum well in which the electrons live. The available states of a single electron thus have energy levels described by

$$\varepsilon(\mathbf{k}) = \frac{\hbar^2 k^2}{2m_{\mathrm{e}}}$$

where $\mathbf{k}$ is the wavevector of the electron so that its momentum is $\mathbf{p} = \hbar\mathbf{k}$. These electrons, are fermions and thus obey the Fermi-Dirac distribution,

$$f(\varepsilon, \mu, T) = \frac{1}{1 + \exp\left(\frac{\varepsilon(\mathbf{k}) - \mu}{k_B T}\right)}$$

In the 0-temperature limit, this distribution reduces to the Heaviside step function, which means that all the electronic states with energies $\varepsilon < \mu$ are occupied and all electronic states above $\varepsilon > \mu$ are empty. Since the free electron dispersion is spherically symmetric with energy monotonically increasing with k, the distribution describes a so-called Fermi sphere of electrons in $\mathbf{k}$-space. This is the Sommerfeld model, from which many electronic properties of a metal such as the Wiedemann Franz law can be derived.

The description of the plasmon will be a direct result of the model when we study the AC conductivity of the metal using the Sommerfeld model. Assuming some momentum

relaxation with time τ, the equation of motion of an electron is

$$
\begin{aligned}
\frac{d\mathbf{p}}{dt} &= -\frac{\mathbf{p}(\omega,t)}{\tau} - e\mathbf{E}(\omega,t) \\
\hbar\frac{d\mathbf{k}}{dt} &= -\frac{\hbar\mathbf{k}(\omega,t)}{\tau} - e\mathbf{E}(\omega,t)
\end{aligned}
$$

where we have implicitly taken an average over the electrons to account for the discrete nature of momentum relaxation. We note that τ is a phenomenological time constant depending on the details of the scattering, in a typical metal this will be due to impurities and phonons. For a typical metal, $\tau \sim 10^{-15}$ s while for very high mobility 2DEG such as those in an AlGaAs/GaAs heterostructure interface, $\tau \sim 10^{-12}$ s.

If we have some oscillatory solution for a driving force $\mathbf{E}(\omega,t) = \mathbf{E}e^{-i\omega t}$ then the solutions will also be oscillatory, $\mathbf{k} = \mathbf{k}e^{-i\omega t}$

$$
\begin{aligned}
-i\omega\hbar\mathbf{k}_1 &= -\frac{\hbar\mathbf{k}_1}{\tau} - e\mathbf{E} \\
\hbar\mathbf{k} &= \frac{\tau e\mathbf{E}}{i\omega\tau - 1}
\end{aligned}
$$

The current is the sum of all the electrons in a small region,

$$
\begin{aligned}
\mathbf{j}(\omega) &= \sum_{\mathbf{k}}(-e)\frac{\hbar\mathbf{k}}{m} \\
&= \sum_{\mathbf{k}}\frac{\tau e^2}{m}\frac{\mathbf{E}}{1 - i\omega\tau} \\
&= \mathbf{E}(\omega)\frac{ne^2\tau}{m}\frac{1}{1 - i\omega\tau}
\end{aligned}
$$

The current is defined $\mathbf{j}(\omega) = \sigma(\omega)\mathbf{E}(\omega)$ and thus the AC conductivity is

$$\sigma(\omega) = \frac{ne^2\tau}{m}\frac{1}{1-i\omega\tau}$$

The limit at low frequencies reduces to the drude DC conductivity, $\sigma(0) = \frac{ne^2\tau}{m}$ while at high frequencies the conductivity is complex and substantially reduced,

$$\sigma(\omega) \to i\frac{ne^2}{m\omega}$$

One can also rewrite this result in terms of the polarizability, and dielectric constant,

$$\mathbf{j}(\omega) = \frac{d\mathbf{P}(\omega)}{dt} = -i\omega\mathbf{P}$$

$$\begin{aligned}
\mathbf{P} &= \chi\mathbf{E} \\
\frac{i}{\omega}\sigma\mathbf{E} &= \chi\mathbf{E}
\end{aligned}$$

$$\begin{aligned}
\varepsilon(\omega) &= \frac{\mathbf{D}(\omega)}{\varepsilon_0\mathbf{E}(\omega)} \\
&= 1 + i\frac{1}{\omega\varepsilon_0}\sigma(\omega) \\
&= 1 - \frac{ne^2}{\varepsilon_0 m\omega^2} \\
&= 1 - \frac{\omega_{p,3D}^2}{\omega^2}
\end{aligned}$$

where we have defined the plasmon frequency $\omega_{p,3D}^2 = \frac{ne^2}{\varepsilon_0 m}$. The interpretation of this result is simple, for frequencies much larger than this plasmon frequency, the electron gas is largely transparent to the propagation of the electromagnetic waves. In most metals, this frequency is in the visible or UV range, which explains the transparency of metals to UV or gamma radiation, even though most metals reflects visible light.

1.2 Circuit Model for 2D plasmons: Kinetic Inductance

Things are drastically different in a 2D material, in which a 2D electron gas lives in the $x - y$ plane. Instead of a single frequency of plasma oscillation, we will be able to find a dispersion relation for plasmon wave propagation. An alternative, simpler semiclassical picture allows us to obtain dispersion relations for the plasmon in terms of a transmission line model, which is useful in that it directly translates to simple design rules capturing the expected plasmon propagation behaviours that one can use to design experiments.

We envision a one-dimensional transmission line made connected at 2 ends, $x = 0$ and $x = L$. Voltages $V(x,t)$ and currents $I(x,t)$ on the line obey the telegrapher's equations,

$$\frac{\partial V}{\partial x} = -L\frac{\partial I}{\partial t} \tag{1.1}$$

$$\frac{\partial I}{\partial x} = -C\frac{\partial V}{\partial t} \tag{1.2}$$

whose solutions necessarily also satisfy the wave equation

$$\frac{\partial^2 V}{\partial t^2} - s^2\frac{\partial V}{\partial x^2} = 0$$

where $s = \frac{1}{\sqrt{LC}}$ is interpreted as the wave velocity. The characteristic impedance of the line is $Z_0 = \sqrt{\frac{L}{C}}$.

Thus we seek to cast the plasmonic wave in similar terms in order to obtain expressions for L and C. The equation of motion of the electronic fluid in a channel of width W is

$$
\begin{aligned}
\frac{\partial \mathbf{v}}{\partial t} &= -\frac{e}{m}\mathbf{E} \\
\left(-\frac{1}{Wen}\right)\frac{\partial I}{dt} &= \frac{e}{m}\frac{\partial V}{\partial x} \\
\frac{\partial V}{\partial x} &= -\frac{m}{ne^2 W}\frac{\partial I}{\partial t}
\end{aligned}
\tag{1.3}
$$

We identify this inductance as the kinetic inductance

$$
L_k = \frac{m}{ne^2 W}
\tag{1.4}
$$

. It's nature is substantially different from that of the magnetic inductance, in which changes in current are resisted by the driving force having its energy stored in magnetic fields: Here, the energy is stored in the kinetic energy of the electrons instead. A much greater detailed description of kinetic inductance and a related concept, plasmonic mass, is given in Section 4.2.

A comparison between the magnetic and kinetic inductance shows the regimes in which each is important. For a 3D metal or semiconductor, we can see that kinetic inductance is completely negligible for realistic carrier densities. However, this is the reverse in 2D conductors: Here, the kinetic inductance is much larger and thus any study of 2D plasmons are kinetic inductance driven: in plasmonic waves, the energy density oscillates

between kinetic and potential energies (as compared to a photonic wave, whose energy density oscillates between magnetic and electrostatic potential energies).

1.3 Circuit Model for 2D plasmons: Capacitance

In much of this work, we will be working with gated plasmons. In this case, the gate acts as the ground so that the capacitance can be related to the local density by

$$n(\mathbf{x}) = \frac{C_g V(\mathbf{x})}{e}$$

where C_g is the geometric capacitance. The continuity equation can then be identified as the second part of the telegraphers equation,

$$
\begin{aligned}
\frac{\partial V}{\partial t} + \frac{\partial V v}{\partial x} &= 0 \\
nWe \frac{\partial V}{\partial t} + V_0 \frac{\partial I}{\partial x} &= 0 \\
\frac{\partial I}{\partial x} &== -C_g W \frac{\partial V}{\partial t}
\end{aligned}
$$

Comparing this to Eq. 1.2, we see that the geometric capacitance is exactly the capacitance that appears in the wave equation.

The plasmonic line's characteristic impedance is

$$Z_0 = \sqrt{L_k/C}$$

$$L_K = \frac{m^*}{n_0 e^2} \frac{1}{W}$$

This means that if we want a 50 ohm line, the widths have to follow this relation,

$$
\begin{aligned}
Z_0 &= \sqrt{\frac{m^*}{n_0 e^2 C_a} \frac{1}{W^2}} \\
W &= \frac{1}{Z_0} \sqrt{\frac{m^*}{n_0 e^2 C_a}}
\end{aligned}
$$

This relationship is satisfied for $W = 20$ um wide sample at 0.2 V back gate, or a density of 1.6×10^{11} cm^2. Using the transmission line velocity we get $v = 7.2 \times 10^5$ m/s, which is much smaller than the speed of light c. It is this small velocity, or equivalently ultra-subwavelength, propagation of plasmons that drives much of the research into this field.

1.4   Circuit Model for 2D plasmons: Resistance

Plasmon propagation almost invariably is plagued with loss and the understanding of the plasmon loss mechanisms is especially crucial in the systems we will be studying experimentally, where the quality factor can be on the order of 10 or less. In fact, we will note here that the loss naturally appears in the model when we consider the AC conductivity of an electron gas since some kind of loss or scattering mechanism is explicitly required in order for the electron gas to even be conducting in the usual sense, as a lossless crystal will undergo Bloch oscillations instead of allowing the electrons to propagate uniformly[1].

The usual model for a lossy transmission line is and RLGC transmission line, which is similar to an LC transmission line described by the telegrapher's equations but with

R in series with the inductance and G in parallel with the capacitance. In this case, the characteristic impedance is still approximately Z_0 and the wave speed is still approximately s. However as the wave propagates, there will be an attenuation $\alpha \propto R$.

The main component of plasmon loss comes from the conductor loss R and not the dielectric loss G, so we will assume that $G = 0$ for the remainder of this thesis. In fact we can explicitly obtain the model by adding a damping term to the equation of motion (Eq. 1.3) to obtain

$$\frac{\partial n}{\partial t} + \frac{\partial (vn)}{\partial x} = 0$$

$$\frac{\partial v}{\partial t} + v\frac{\partial v}{\partial x} + \frac{e}{m_e}E + \frac{v}{\tau_p} = 0$$

Now we proceed to linearize these equations about $U = U_0$, $v = 0$, corresponding to some density and no flow. Also, we make the substitution $n = CU/e$.

$$\frac{\partial v}{\partial t} + \frac{e}{m}\frac{\partial U}{\partial x} + \frac{v}{\tau_p} = 0$$

$$\frac{\partial U}{\partial t} + U_0\frac{\partial v}{\partial x} = 0$$

Solving this we get the very familiar wave equation, with wave velocity $c = \sqrt{\frac{eU_0}{m}}$

$$\frac{\partial^2 v}{\partial t^2} + \frac{e}{m}\frac{\partial^2 U}{\partial x\partial t} + \frac{1}{\tau}\frac{\partial v}{\partial t} = 0$$

$$\frac{\partial^2 U}{\partial t\partial x} + U_0\frac{\partial^2 v}{\partial x^2} = 0$$

$$\frac{\partial^2 v}{\partial t^2} + \frac{1}{\tau}\frac{\partial v}{\partial t} = \frac{e}{m}U_0\frac{\partial^2 v}{\partial x^2}$$

Assume $v = v_A e^{i(kx - \omega t)}$, we can get a dispersion relation, which allows us to solve,

$$\omega^2 + \frac{1}{\tau} i\omega - \frac{e}{m} U_0 k^2 = 0$$

$$
\begin{aligned}
\omega &= \frac{-\frac{i}{\tau} \pm \sqrt{\frac{4e}{m} U_0 k^2 - \frac{1}{\tau^2}}}{2} \\
&= \pm \sqrt{\frac{e}{m} U_0 k^2 - \frac{1}{4\tau^2}} - \frac{i}{2\tau}
\end{aligned}
$$

Plugging back into our solution, we see that

$$v = v_A e^{i\left(kx - \sqrt{\frac{e}{m} U_0 - \frac{1}{4\tau^2}} t\right)} e^{-\frac{t}{2\tau}}$$

How does this apply to the case of a transmission line? Rearranging,

$$
\begin{aligned}
\pm \sqrt{\frac{m}{eU_0} \left[\left(\omega + \frac{i}{2\tau}\right)^2 + \frac{1}{4\tau^2} \right]} &= k \\
k &= \pm \sqrt{\frac{m}{eU_0} \left[\omega^2 + \frac{i}{\tau} \omega \right]}
\end{aligned}
$$

The solution is thus

$$v = v_A e^{i(k_{re}x - \omega t)} e^{-k_{im}x}$$

For large enough τ, both k_{im} and k_{re} have the same sign, which describes the propagation of decaying waves decaying waves. The propagation constant in a transmission line is $\gamma = \pm\sqrt{(r_s + i\omega L)(i\omega C)} = \alpha + i\beta = \pm ik = \sqrt{-\frac{m}{eU_0}\left[\omega^2 + \frac{i}{\tau}\omega\right]}$. Comparing coefficients, $i\omega r_s C = -\frac{im\omega}{\tau eU_0}$ and $LC = \frac{m}{eU_0}$. Note the sign convention, which arises from the convention of phasors in electrical engineering going as $e^{i\omega t}$, instead of $e^{-i\omega t}$. In the more familiar physics convention if we had used $e^{-i\omega t}$ the constant would be $\gamma = \pm\sqrt{(r_s - i\omega L)(-i\omega C)} = \pm ik = \sqrt{-\frac{m}{eU_0}\left[\omega^2 + \frac{i}{\tau}\omega\right]}$, and comparing coefficients, $LC = \frac{m}{eU_0}$ and $Cr_s = \frac{m}{eU_0\tau}$. Unsurprisingly, the resistance is directly given by the scattering time constant τ and thus, in this model, is directly given by the mobility of the system.

1.5   Structure of the Dissertation

The key concepts of kinetic inductance and quantum and geometric capacitances in the context of 2D conductors has been introduced. In the next chapter, we will study the dispersion relations of 2D plasmons in greater detail, to try to tease out corrective and additional terms that may arise. In Chapter 3 we demonstrate the use of these plasmons in band engineering plasmonic crystals made with graphene. In Chapter 4, we examine how kinetic inductance applies to 2D conductors in the calculation of the noise spectrum with the fluctuation dissipation theorem. The work in Chapters 3 and 4 have been largely published in references [2] and [3] respectively. Lastly, in Chapter 5, we will describe

the measurement of nonreciprocal plasmons in a drifting electron gas, using the ultrahigh-mobility GaAs / AlGaAs heterostructure as an example system in which such nonreciprocal plasmons can be measured. We will also discuss the possibility of obtaining reflection gain of drifting plasmons, and possibilities of measuring this phenomenon in graphene.

Chapter 2

2D Plasmons: Dispersion Relations, Corrections and Additional Terms

In the previous chapter, we have derived plasmon dispersion relations even in the presence of loss, which we assume to be small, even though this assumption is not always experimentally true. In this section, we study several other terms which we expect to contribute to the plasmonic dispersion relations, some of which will be too small to cause an experimentally observable effect on the dispersion relation.

2.1 Hydrodynamic Terms

The equations of motion are

$$\frac{\partial n}{\partial t} + \frac{\partial (vn)}{\partial x} = 0$$

$$\frac{\partial v}{\partial t} + \frac{\partial x}{\partial t}\frac{\partial v}{\partial x} + \frac{e}{m_e}E + \frac{v}{\tau_p} = 0$$

Define U to be the local gate voltage relative to the channel, which means $E = \frac{\partial U}{\partial x}$ without the minus sign. Substituting $n = \frac{CU}{e}$.

$$\frac{\partial v}{\partial t} + v\frac{\partial v}{\partial x} + \frac{e}{m}\frac{\partial U}{\partial x} + \frac{v}{\tau_p} = 0$$
$$\frac{\partial U}{\partial t} + \frac{\partial Uv}{\partial x} = 0$$

First we do the steady state under a constant drift current I_0. In this case there is no time dependence, so the second line gives $U_0 v_0 = \text{const} = \frac{en_0}{C}v_0 = -\frac{I_0}{AC}$. So we can rewrite the first equation by using $v_0 = \frac{Q}{U_0}$

$$v_0\frac{\partial v_0}{\partial x} + \frac{e}{m}\frac{\partial U_0}{\partial x} + \frac{v_0}{\tau_p} = 0$$
$$-\frac{Q^2}{U_0^3}\frac{\partial U_0}{\partial x} + \frac{e}{m}\frac{\partial U_0}{\partial x} + \frac{Q}{U_0\tau_p} = 0$$
$$\frac{\partial U_0}{\partial x} = -\frac{Q}{\tau_p U_0\left(\frac{e}{m} - \frac{Q^2}{U_0^3}\right)} = -\frac{QU_0^2}{\tau_p\left(\frac{e}{m}U_0^3 - Q^2\right)}$$

This equation cannot be solved analytically. However, in the triode regime, we can simply take $\frac{dU_0}{dx}$ to be constant

$$
\begin{aligned}
U_0(x) &= U_0(0) + \frac{dU_0}{dx}x \\
v_0(x) &= \frac{Q}{U_0(0) + \frac{dU_0}{dx}x} \\
\frac{dv_0}{dx} &= \frac{Q}{\left(U_0(0) + \frac{dU_0}{dx}x\right)^2}\frac{dU_0}{dx}
\end{aligned}
$$

The linearized equations about $U = U_0 + u_1$, $v = v_0 + v_1$ are

$$
\frac{\partial v}{\partial t} + v_0(x)\frac{\partial v}{\partial x} + v\frac{\partial v_0}{\partial x}(x) + \frac{e}{m}\frac{\partial U}{\partial x}(x) + \frac{v}{\tau_p} = 0
$$

$$
\frac{\partial U}{\partial t} + U_0(x)\frac{\partial v}{\partial x} + U\frac{\partial v_0}{\partial x}(x) + v_0(x)\frac{\partial U}{\partial x} + v\frac{\partial U_0}{\partial x}(x) = 0
$$

$$
\frac{\partial v}{\partial t} + \left(v_0(0) - \frac{1}{U_0^2}\frac{\partial U_0}{\partial x}x\right)\frac{\partial v}{\partial x} - v\left(\frac{1}{U_0^2}\frac{\partial U_0}{\partial x}\right) + \frac{e}{m}\frac{\partial U}{\partial x}(x) + \frac{v}{\tau_p} = 0
$$

$$
\frac{\partial U}{\partial t} + \left(U_0(0) + \frac{\partial U_0}{\partial x}x\right)\frac{\partial v}{\partial x} - \frac{1}{U_0^2}\frac{\partial U_0}{\partial x}U + \left(v_0(0) - \frac{1}{U_0^2}\frac{\partial U_0}{\partial x}x\right)\frac{\partial U}{\partial x} + v\frac{\partial U_0}{\partial x}(x) = 0
$$

This has solutions given by substituting $v = \tilde{v}e^{i(kx+\omega t)}$ and $U = \tilde{U}e^{i(kx+\omega t)}$ (note the time dependence, which is the convention we choose so that negative impedance is capacitive and positive is inductive) to get a matrix equation, and using the slowly varying envelope approximation, where we throw away all the terms of $\frac{\partial k}{\partial x}$.

$$
\frac{\partial U}{\partial x} = i\left(k + x\frac{\partial k}{\partial x}\right)Ue^{i(kx+\omega t)}
$$

Using the slowly varying envelope approximation,

$$i\omega\tilde{v} + v_0 ik\tilde{v} + \tilde{v}\frac{\partial v_0}{\partial x} + ik\frac{e}{m}\tilde{U} + \frac{\tilde{v}}{\tau_p} = 0$$

$$i\omega\tilde{U} + ikU_0\tilde{v} + \tilde{U}\frac{\partial v_0}{\partial x} + ikv_0\tilde{U} + \tilde{v}\frac{\partial U_0}{\partial x} = 0$$

$$\begin{bmatrix} i\omega + ikv_0 + \frac{\partial v_0}{\partial x} + \frac{1}{\tau_p} & ik\frac{e}{m} \\ ikU_0 + \frac{\partial U_0}{\partial x} & i\omega + ikv_0 + \frac{\partial v_0}{\partial x} \end{bmatrix} \cdot \begin{bmatrix} \tilde{v} \\ \tilde{U} \end{bmatrix} = \mathbf{0}$$

Solving this characteristic equation gives the dispersion relation.

$$\det \begin{bmatrix} i\omega + ikv_0 - \frac{Q}{U^2(x)}\frac{\partial U_0}{\partial x} + \frac{1}{\tau_p} & ik\frac{e}{m} \\ ikU_0 + \frac{\partial U_0}{\partial x} & i\omega + ikv_0 - \frac{Q}{U^2(x)}\frac{\partial U_0}{\partial x} \end{bmatrix} = \mathbf{0}$$

The characteristic equation gives the dispersion relation that is quadratic in k and is easily solved. While the solution will have many terms due to the additional terms with derivatives of U_0, in the lossless case where $\tau \to \infty$, we can simplify this greatly by noting that $\frac{\partial U_0}{\partial x} = 0$ which means that the electron density is constant across the electron gas. We also

16

use the substitution $s = \sqrt{\frac{eU_0}{m}}$,

$$
\begin{bmatrix} i\omega + ikv_0 & ik\frac{e}{m} \\ ikU_0 & i\omega + ikv_0 \end{bmatrix} \cdot \begin{bmatrix} \tilde{v} \\ \tilde{U} \end{bmatrix} = \mathbf{0}
$$

$$
-(\omega + kv_0)^2 + k^2 s^2 = 0
$$

$$
\omega + kv_0 = \pm ks
$$

$$
-v_0 \pm s = \frac{\omega}{k}
$$

The situation is thus that of waves traveling as velocity s, being carried along by an additional velocity v_0. We can rewrite this for convenience, $k_\pm = \omega/(-v_0 \pm s)$ where $s = \sqrt{\frac{eU_0}{m}}$. Thus the general solution is

$$
U = U_+ e^{i(k_+ x + \omega t)} + U_- e^{i(k_- x + \omega t)}
$$

$$
\omega \tilde{U} + kU_0 \tilde{v} + kv_0 \tilde{U} = 0
$$

$$
\omega \tilde{U} + kU_0 \tilde{v} - i\tilde{U}\frac{\partial v_0}{\partial x} + kv_0 \tilde{U} + -i\tilde{v}\frac{\partial U_0}{\partial x} = 0
$$

So the general solution is

$$
U(x,t) = -\frac{k_+ v_0 + \omega - i\frac{\partial v_0}{\partial x}}{k_+ U_0 - i\frac{\partial U_0}{\partial x}} U_+ e^{i(k_+ x + \omega t)} - \frac{k_- v_0 + \omega - i\frac{\partial v_0}{\partial x}}{k_- U_0 - i\frac{\partial U_0}{\partial x}} U_- e^{i(k_- x + \omega t)}
$$

In this description the wavenumbers k_+ describes waves that are propagating backwards, while k_- describes waves that are propagating forwards.

This observation that the system admits waves with different propagation velocities in the forwards and backwards directions is significant: the transmission line is nonreciprocal and may be used as the key nonreciprocal component in devices such as microwave gyrators or isolators. We have experimentally observed this in the GaAs / AlGaAs heterostructure and and will explore this further in chapter 5.

2.2 Quantum Capacitance

In this discussion, quantum capacitance refers to the capacitance that arises due to an average increase in the electron energy levels as the system becomes more and more populated with electrons. This increase in energy necessary to add an electron to the system manifests itself as a capacitance which is in series with the geometric capacitance (an example 1D system to show this is discussed in appendix C). In typical 3D semiconductor systems, this effect is entirely negligible (i.e. the quantum capacitance is extremely large) because most of the valence band electrons live near the band edge and occupy about the same energy states. However, for lower dimentional systems with low density of states, we expect that the quantum capacitance can be small enough for its effect to be measureable.

To compute the quantum capacitance of a 2D electron gas, we only need to calculate the total individual electron energy and take the appropriate derivative. If we consider just a isotropic parabolic 2DEG with effective mass m_e^* with constant density of states is given by $\frac{gm_e^*}{2\pi\hbar^2}$, we can find the chemical potential by solving the equation

$$n = \int D(E)f(E,\mu,k_BT)dE$$

for some fixed electron density n. In experiment, this n might be fixed by a voltage applied to the gate. Then the total energy per unit area of the system is given by

$$E = \int E \cdot D(E) f(E, \mu, k_B T) dE$$

and the capacitance is $dE/dQ = \frac{Q}{C} \implies C = \frac{Q}{dE/dQ}$. At zero temperature, we can see that it reduces to the analytic result $C = \frac{g m_e^* e^2}{\pi \hbar^2}$.

2.3 Magnetic Field

In this section we study the case of a plasmon with magnetic field. We expect that the magnetic field can perturb the motion of electrons, which could imply a change in the plasmon propagation characteristics. In particular, it is well known that magnetic materials are also nonreciprocal, so we might anticipate some novel interactions between the magnetic field and the non-magnetic nonreciprocity of the electron gas with drift. In this case the electron equations of motions are

$$\frac{\partial n}{\partial t} + \nabla \cdot (n\mathbf{v}) = 0$$

$$\frac{\partial \mathbf{v}}{\partial t} + (\mathbf{v} \cdot \nabla) \mathbf{v} + \frac{e}{m_e} (\mathbf{E} + \mathbf{v} \times \mathbf{B}) = 0$$

Suppose $\mathbf{v}$ is small so that we can ignore the convective terms for now. Then

$$\frac{\partial n}{\partial t} + \nabla \cdot (n\mathbf{v}) = 0$$

$$\frac{\partial \mathbf{v}}{\partial t} + \frac{e}{m_e} \left(-\nabla U + \mathbf{v} \times \mathbf{B} \right) = 0$$

Without applying an electric field, $\mathbf{E} = -\nabla U$, and $n = -\frac{CU}{e}$. With these definitions we require $U, U_0 < 0$. So if we linearize,

$$
\begin{aligned}
\frac{\partial U}{\partial t} + U_0 \nabla \cdot \mathbf{v} &= 0 \\
\frac{\partial \mathbf{v}}{\partial t} + \frac{e}{m_e} \left(-\nabla U + \mathbf{v} \times \mathbf{B} \right) &= 0
\end{aligned}
$$

Now put in some time dependence, following the EE convention, $v = \tilde{\mathbf{v}} e^{i(\mathbf{k} \cdot \mathbf{x} + \omega t)}$ and $U = \tilde{U} e^{i(\mathbf{k} \cdot \mathbf{x} + \omega t)}$,

$$
\begin{aligned}
i\omega \tilde{U} + iU_0 \mathbf{k} \cdot \tilde{\mathbf{v}} &= 0 \\
i\omega \tilde{\mathbf{v}} + \frac{e}{m_e} \left(-i\mathbf{k}\tilde{U} + B_0 \tilde{\mathbf{v}} \times \hat{z} \right) &= 0
\end{aligned}
$$

Let us expand this into scalar equations,

$$
\begin{aligned}
\frac{\omega \tilde{U}}{U_0} + (k_x v_x + k_y v_y) &= 0 \\
\omega v_x + \frac{e}{m_e} \left(-k_x \tilde{U} - iB_0 v_y \right) &= 0 \\
\omega v_y + \frac{e}{m_e} \left(-k_y \tilde{U} + iB_0 v_x \right) &= 0
\end{aligned}
$$

The determinant of the matrix must be 0,

$$-\frac{B_0^2 e^2}{m_e^2} + \frac{eU_0}{m_e}k^2 + \omega^2 = 0$$

This is the case with no drift, where there is an additional term that arises from the magnetic field. A plot of this is shown in Fig. 2.1.

Now if we put back the convective terms,

$$
\frac{\partial U}{\partial t} + \nabla \cdot (U\mathbf{v}) = 0
$$

$$
\frac{\partial \mathbf{v}}{\partial t} + (\mathbf{v} \cdot \nabla)\mathbf{v} + \frac{e}{m_e}(\mathbf{E} + \mathbf{v} \times \mathbf{B}) = 0
$$

Linearizing around nonzero $\mathbf{v_0}$ and without loss of generality setting $\mathbf{v_0}$ to be in the x direction,

$$
\frac{\partial U}{\partial t} + U_0 \nabla \cdot \mathbf{v} + \mathbf{v_0} \cdot \nabla U = 0
$$

$$
\frac{\partial \mathbf{v}}{\partial t} + (\mathbf{v_0} \cdot \nabla)\mathbf{v} + \frac{e}{m_e}(-\nabla U + \mathbf{v} \times \mathbf{B}) = 0
$$

Put in time dependence,

$$
i\omega\tilde{U} + iU_0\mathbf{k} \cdot \tilde{\mathbf{v}} + i\tilde{U}v_0 k_x = 0
$$

$$
i\omega\tilde{\mathbf{v}} + v_0 i k_x \tilde{\mathbf{v}} + \frac{e}{m_e}\left(-i\mathbf{k}\tilde{U} + B_0 \tilde{\mathbf{v}} \times \hat{z}\right) = 0
$$

Expanding into scalar equations,

$$
\frac{(\omega + v_0 k_x)\tilde{U}}{U_0} + (k_x v_x + k_y v_y) = 0
$$

$$
\omega v_x + v_0 k_x v_x + \frac{e}{m_e}\left(-k_x \tilde{U} - i B_0 v_y\right) = 0
$$

$$
\omega v_y + v_0 k_x v_y + \frac{e}{m_e}\left(-k_y \tilde{U} + i B_0 v_x\right) = 0
$$

21

$v_0 = 0$ m/s

$v_0 = 1e6$ m/s

f / GHz

f / GHz

k / m^{-1} x 10^5

k / m^{-1} x 10^5

0T
0.01T
0.02T
0.03T
0.04T

Figure 2.1: Plots showing the dispersion along the k_x direction for the case with drift and without. The 2DEG is assumed to have a density of 1.6×10^{11} cm^{-1}, which gives an $s = 7.2 \times 10^5$ ms^{-1}.

Now this is simply a replacement of ω with $\omega + v_0 k_x$ from the previous equations. Solving, we get that the dispersion relation is

$$-\frac{B_0^2 e^2}{m_e^2} + \frac{eU_0}{m_e}k^2 + (\omega + v_0 k_x)^2 = 0$$

Again, we can plot this dispersion relation, which is similar to the case with no drift. However, interestingly, there is a region of negative dispersion very close to $k = 0$, but it remains to be seen if this is experimentally feasible.

Chapter 3

Graphene Plasmonic Crystals

In this chapter we will study graphene plasmon crystals, which are sheets of graphenes in which the plasmon dispersion has been modified by a structural periodicity. We introduce such periodicity by patterning a hexagonal array of apertures in a graphene sheet. The interaction of the plasmons with the graphene periodicity forms a plasmonic band structure. This is demonstrated by resonantly coupling a far-infrared light into particular plasmonic modes belonging to a unique set of plasmonic bands, where the light selects these specific modes because the spatial symmetry of the radiation field matches that of the plasmons within those modes. This work is a step toward graphene plasmon band engineering, paving avenues for novel graphene plasmonic devices by demonstrating the applicability of concepts from photonic crystals such as the possibility of plasmon band engineering and utilization of symmetry-based plasmon band selection rule.

One can imagine a variety of ways to introduce structural periodicity in a continuous graphene medium. The hexagonal lattice of apertures in our work is one proof-of-concept

realization of the medium periodicity. We fabricate four graphene plasmonic crystals, which we call GPC1 to GPC4 (Figure 1a), by etching out hexagonal lattices of circular (GPC1) or hexagonal shape apertures (GPC2 to GPC4) via photolithography in four separate regions of the same 1.5×1.5 cm^2) graphene sheet. This graphene sheet, which is grown by chemical vapor deposition (CVD) and is transferred onto a 289 nm SiO$_2$/381 μm Si substrate, exhibits the typical Raman spectrum (Figure 1b) of monolayer graphene [4, 5]. The hexagonal lattice geometry of each plasmonic crystal occupying an area of 2×2 mm^2 is characterized by the lattice constant a, the aperture shape that is circular or hexagonal, and the aperture size (diameter D in case of circular apertures, edge-to-opposite-edge distance $D\prime$ in the case of hexagonal apertures). The geometric parameters are in the micrometer range; for instance, a ranges from 3 to 6 μm. An optical micrograph and a scanning electron microscopy (SEM) image of GPC1 ($a \sim 3$ μm; $D \sim 2$ μm) are in Figures 1c,d. The map of the integrated Raman 2D peak intensity [4, 6] from 2630 to 2730 cm^{-1} (Figure 1e) also confirms the hexagonal lattice in the graphene.

We also leave a certain region unpatterned (area: 1.0×0.5 cm^2) in the same graphene sheet, as its interaction with far infrared light provides a comparison to the interaction of plasmonic crystals with far infrared light. On this unpatterned graphene, we also perform a Hall transport measurement via the four-probe Van der Pauw method from which we determine the charge carrier type (holes), its concentration $n = 1.1 \times 10^{13}$ cm^{-2}, and mobility $\mu = 1360$ cm^2/Vs. These values correspond to a Fermi level $E_F = -0.38$ eV and carrier scattering time $\tau = 5 \times 10^{-14}$ s. E_F and τ are important characteristics that influence the detailed behavior of graphene plasmons. While E_F and τ spatially vary in large-area graphene14 and also may assume degraded values in the patterned graphene plasmonic
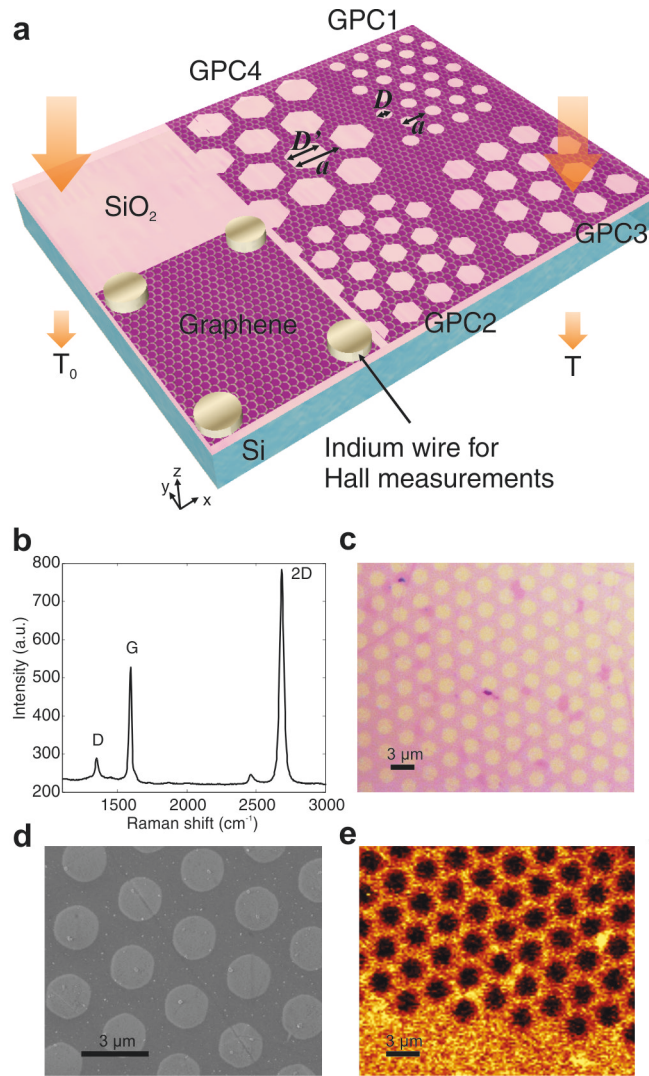
Figure 3.1: a. Illustration (not drawn to scale) of our graphene sample on SiO2/Si substrate, containing four graphene plasmonic crystals: GPC1 ($a \sim 3$ μm, $D \sim 2$ μm), GPC2 ($a \sim 4$ μm, $D\prime \sim 3$ μm), GPC3 ($a \sim 5$ μm, $D\prime \sim 4$ μm), GPC4 ($a \sim 6$ μm, $D\prime \sim 5$ μm), an unpatterned graphene region, and bare SiO2/Si region uncovered by graphene. T [T0] is the light intensity transmitted through a crystal [bare SiO_2/Si] in FTIR. b. Typical Raman spectrum of the graphene sample in the unetched area. c. Optical image, d. SEM image e. integrated graphene Raman 2D peak intensity map from 2630 to 2730 cm^{-1} of GPC1, with dark areas indicating apertures.

crystals due to the edge disorder introduced at the boundaries of the apertures [7], their grossly measured values in the unpatterned region give a rough feel for their values in the crystal regions and signify certain characteristics of the graphene sample. For instance, our graphene sample is strongly doped (with holes), and plasmonic quality $Q = \omega\tau \sim 2$ at 6 THz.

The length scales of the hexagonal lattice parameters a, D, and $D\prime$ are comparable to the graphene plasmonic wavelengths in the far-infrared region, where graphene plasmons emerge conspicuously [8]. Hence, plasmons are scattered by the lattice, and their dispersion relation is transformed from the continuous dispersion curve of unpatterned graphene16 into a plasmonic band structure, as seen theoretically [9, 10]. We first show the plasmonic band structure of our hexagonal lattice by simulation, by solving Maxwell's equations via the finite element method with appropriate boundary conditions using COMSOL Multiphysics. Here graphene is modeled as a 0.5 nm thick conducting boundary layer with a conductivity corresponding to the intraband transitions at room temperature:

$$\sigma\left(\omega, E_F, \tau\right) = -i\frac{e^2 E_F}{\pi\hbar^2}\frac{1}{\omega - i/\tau}$$

Bloch boundary conditions were used to represent the periodic structure. The material properties of the substrate are obtained from tabulated data.19 The simulated band structure for GPC1 is displayed in Figure 2a (horizontal axis: plasmonic wavenumber, k_p; vertical axis: frequency, f), where the 11 lowest lying bands are shown along the high-symmetry points in reciprocal space. For this particular simulation, we use $E_F = -0.38$ eV, obtained in the unpatterned region, as the exact value of E_F of the crystal is

unknown. Simulations with differing E_F values reveal that the band diagram scales vertically in proportion to $\sqrt{|E_F|}$, which is a key signature of graphene plasmons [8, 11]. For example, Figure 2b shows this E_F dependency of the degenerate mode frequency of plasmonic bands 5 and 6 at the Γ-point. To demonstrate the plasmonic band formation in the graphene plasmonic crystal, we perform Fourier transform infrared spectroscopy (FTIR) at room temperature by normally irradiating an unpolarized far-infrared plane wave along the zaxis onto the device lying in the x−y plane. The wave vector k of the normally incident light has no component in the plane of the graphene, yet the corresponding $k_x = k_y = 0$ line can still excite plasmonic modes at the Γ point ($k_p = 0$) on the bands; such phase-matching and resultant plasmonic excitation would not be possible in unpatterned graphene, which exhibits a continuous plasmonic dispersion relation with no plasmonic band formation.

Among all available Γ-point plasmonic modes, only two pairs of degenerate Γ-point modes belonging to bands 5 and 6 and bands 10 and 11 can be excited because the spatial symmetry of these specific plasmonic modes matches the spatial symmetry of the fields of the normally incident plane waves [12, 13]. All other Γ-point modes behave differently than the radiation fields under symmetry operations (such as reflections with respect to planes parallel to the z-axis or rotations about the z-axis) and thus cannot be excited despite their phase matching to the normally incident wave. To help appreciate this, we illustrate the symmetries of all Γ-point plasmonic modes of the 11 lowest-lying bands by displaying the simulated spatial profiles of their electric field in the z-direction, $E_{p,z}$, just above the graphene (Figure 2c). The Γ-point plasmonic mode belonging to band 7, for example, has a 120° rotational symmetry about the z-axis, a symmetry that radiation fields do not possess, and thus it cannot be excited.
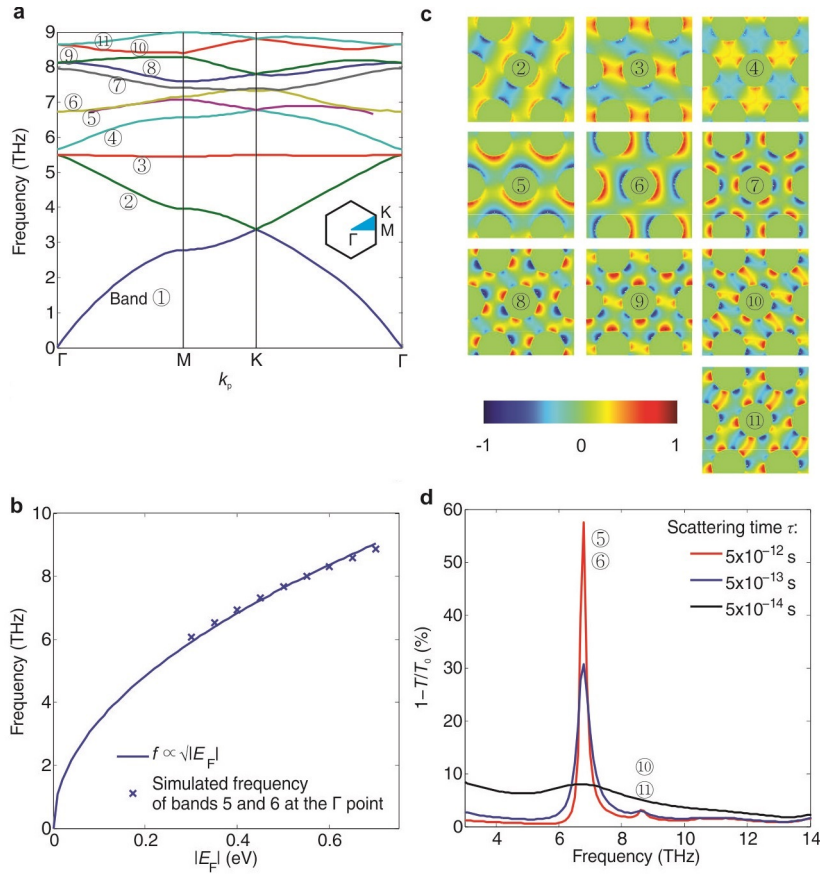
Figure 3.2: a. Simulated band structure of GPC1 ($E_F = -0.38$ eV) along high symmetry points of a hexagonal reciprocal lattice (inset). b. Simulated frequencies of degenerate Γ-point plasmonic modes on bands 5 and 6 with varying E_F and a least-squares fit to $f \propto \sqrt{|E_F|}$. c. Simulated $E_{p,z}$, just above graphene for each Γ-point mode. Color bar shows normalized field strength. d. Simulated extinction spectra of GPC1 for various τ values. For (c) and (d) $E_F = -0.38$ eV is used as in (a).

This symmetry-based selection rule can be formally proved. The hexagonal lattice possesses the C6v point group symmetry, and thus, each Γ-point mode hosted by the lattice exhibits definite symmetry transformation properties under any symmetry operation belonging to the C6v group. However, one can show that the symmetry transformation

properties of only the degenerate Γ-point modes on bands 5 and 6 and those on bands 10 and 11 match the symmetry transformation properties of normally incident plane waves, being described by the same irreducible representation of the C6v group [13, 14]. A more detailed explanation is given in B.

Simulation supports this selective plasmonic excitation. We solve Maxwell's equations with a plane-wave excitation to obtain the extinction, $1 - T/T_0$ (T and T_0 are the light intensity transmitted through the on-substrate graphene device of concern and through the substrate only, respectively; Figure 1a), which indicates the degree of absorption or reflection by the device. Figure 2d displays simulated extinction spectra of GPC1 with $E_F = -0.38$ eV for differing values of τ. Simulation with either x- or y-polarized excitation light gives the same result. For $\tau = 5 \times 10^{-12}$ s this relatively long scattering time is feasible with high-mobility exfoliated graphene and the extinction spectrum exhibits two peaks, confirming the selective excitation; the tall 6.8 THz peak (small 8.6 THz peak) is due to the excitation of the degenerate Γ-point plasmonic modes exactly at the same frequency on bands 5 and 6 (bands 10 and 11) in Figure 2a. These peaks, which can also be designed to occur in the mid-infrared [15], are due to Fano resonances between the plasmon modes and direct transmission through the graphene, similar to the Fano resonance in photonic crystal slabs [16]. With decreasing τ that lowers the plasmon quality factor[17, 18], each peak grows shorter and broader in simulation. For $\tau = 5 \times 10^{-14}$ s that is commensurate with the mobility of our CVD-grown graphene, the peak due to the degenerate Γ point on bands 5 and 6 remains observable at a slightly lowered frequency (6.7 THz), while the peak due to the degenerate Γ point on bands 10 and 11 is unresolvable. Simulated extinction spectra with different geometric parameters show the same behavior;

in the low scattering regime, the extinction shows multiple peaks corresponding to a subset of Γ-point plasmonic modes allowed by the symmetry selection rule; in the high scattering regime (as in CVD graphene), a single broad peak appears, typically around the originally dominant peak.

Our work employs lower-mobility CVD graphene with $\tau = 5 \times 10^{-14}$ s, for its large area is amenable to maximal coupling with the far-infrared beam from an Ever-Glo IR source (beam diameter: ~8.75 mm). To ensure the measurement of only one particular plasmonic crystal under test, a mask with a pinhole (diameter ~2 mm) is aligned right behind the particular crystal to permit only its signal transmitted. Thus, we expect from the simulation that the extinction spectrum will exhibit a single broad peak. In fact, the measured spectrum (Figure 3a, blue) of a GPC1 in the frequency range of 3–14 THz (above the lower cutoff frequency of a Thermo Fisher FTIR6700 system used and below the absorption bands of SiO2) exhibits a single broad peak near 6 THz with an overall decreasing background, in agreement with the shape of the extinction spectrum simulated with $\tau = 5 \times 10^{-14}$ s. (The measurement is done in a nitrogen atmosphere with a polyethylene windowed far-IR deuterated triglycine sulfate detector; the transmission spectrum of nitrogen is separately measured, and this background spectrum is subtracted from every device spectrum.) This peak is due to the excitation of the degenerate Γ-point plasmonic modes on bands 5 and 6. The emergence of the peak demonstrates the band structure formation by the periodic structuring. This is because in unpatterned graphene the plasmonic dispersion curve does not form bands and thus cannot meet with the $k_x = k_y = 0$ line representing the normally incident light. This lack of coupling between the light and

plasmons in unpatterned graphene is clearly seen in the measured extinction of the unpatterned graphene region (Figure 3a, red). The monotonic spectrum is due to the background interaction between the light and graphene free carriers [11]; no peak is observed due to the lack of light–plasmon coupling.

We can obtain the extinction peak frequencies by fitting the experimental spectra to a single-peak Fano resonance line shape

$$1 - \frac{T}{T_0} = A T_B(\omega) \frac{\left(q_f + \frac{2(\omega - \omega_0)}{\Gamma_P} \right)^2 + b}{1 + \left(\frac{2(\omega - \omega_0)}{\Gamma_P} \right)^2}$$

where fitting parameters are A (amplitude), q_f (Fano parameter), Γ_p(plasmon damping rate), ω_0 (natural frequency), and b (screening parameter). Here T_B is the background extinction spectrum obtained experimentally from transmission through unpatterned graphene (Figure 3a, red). This single Fano resonance fit well approximates the single broad extinction peak in each graphene plasmonic crystal in the heavy carrier scattering regime (Supporting Information), and the R2 statistics of the fits are in the range of 0.88−0.95. The peak frequency obtained this way, 6.3 THz, is close to the simulated peak frequency at 6.7 THz. The ~5% difference from the simulation is largely due to spatial variations in E_F; that is, $E_F = -0.38$ eV used in the simulation is from the unpatterned graphene region, while the crystal region under test in general assumes a different E_F value.

The observation of a single plasmon peak is robust across the remaining three plasmonic crystals with differing hexagonal lattice geometries (Figure 3b−e), further affirming the formation of the plasmonic band structure by the periodic patterning. As expected,
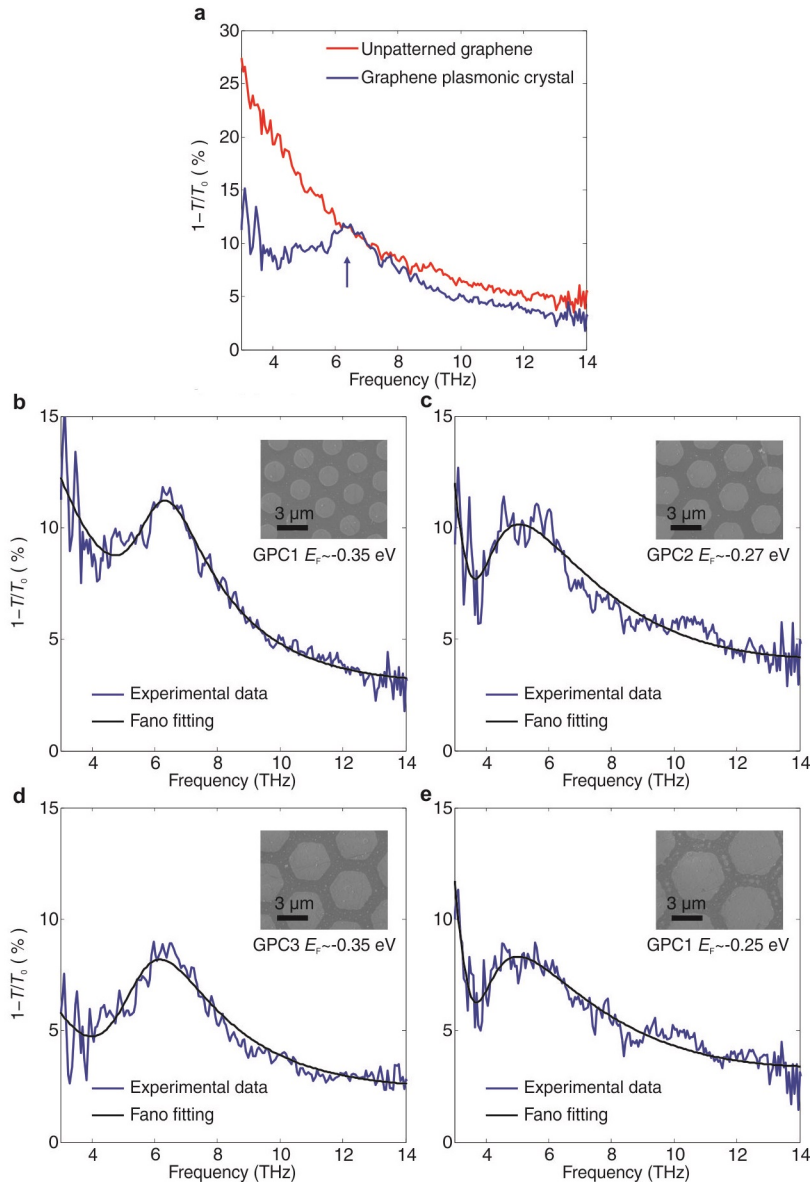
Figure 3.3: a. Extinction spectra of unpatterned graphene (red) and GPC1 (blue), measured by FTIR spectroscopy. b–e. Extinction spectra (blue) of GPC1–GPC4, least-squares fits (black) to an expression based on a Fano resonance. The grossly estimated value of E_F by simulation peak fitting (main text) is indicated for each crystal. The insets are SEM images of the crystals.

the peak frequency varies from device to device because the band structure is altered with the lattice geometry. In our setup, the dependency of the peak frequency solely on geometric parameters (Supporting Information) cannot be closely examined, due in part to the photolithographic inaccuracy in controlling the geometric parameters to submicrometer precision and more fundamentally because E_F varies from device to device and from region to region even within a single device (spatial variations of E_F on CVD graphene can be on the order of 0.1 eV [19, 20]). In fact, we estimate the gross effective E_F of each plasmonic crystal by matching the peak frequency between the measured and simulated spectrum, where the simulation uses E_F as a fitting variable and size and shape of the apertures estimated from the SEM as fixed parameters (τ is kept at ~5 × 10−14 s in this simulation because extinction peak frequencies are not sensitive to τ, as far as τ varies within the range expected for CVD graphene); the device-to-device variation of EF so estimated is up to ~0.1 eV (Figure 3b−e).

We further confirm the plasmonic origin of the observed peak by upshifting the overall $|E_F|$ distribution across the entire sample containing the four crystals via global chemical doping of holes and by verifying if the peak frequency of each crystal increases. This method is beneficial in the face of the device-todevice variation of E_F since it does not require the exact knowledge of the spatial distribution of E_F. After chemically hole-doping the sample by exposure to 70% HNO_3 vapor for 1 min, which increases the measured E_F from −0.38 to −0.55 eV in the unpatterned region, the measured peak frequency in every crystal shifts upward consistently (Figure 4), reaffirming the plasmonic origin of the spectral peaks. Incidentally, the frequency upshift factor indicated in Figure 4 is not constant among the devices because the predoping E_F spatial profile is nonuniform, doping

itself may not be perfectly uniform, and the ex situ doping procedure may cause a slightly different crystal position to be probed by the FTIR before and after doping.
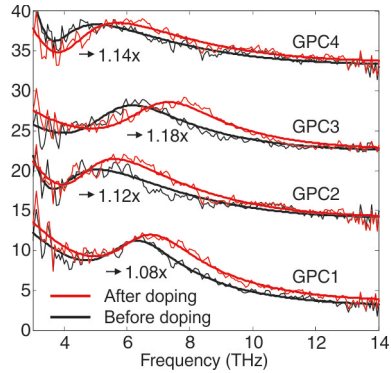
Figure 3.4: Extinction spectra (thin lines) of the four graphene plasmonic crystals before (black) and after (red) hole doping. The factor by which the peak frequency increases is shown for each crystal. Bold lines are least-squares fits to an expression based on the Fano resonance. A vertical cumulative offset of 10% is added between the spectra from different crystals for clarity.

Chapter 4

Plasmonic Mass and Fluctuation Dissipation Theorem

4.1 Introduction

The phenomenon of Johnson-Nyquist noise [21, 22] is not only of great importance for its own sake, but it also offers a prominent example of fluctuation-dissipation relation [23, 24]. The fluctuation-dissipation theorem dictates that the power spectral density of the Johnson-Nyquist current noise in a conductor is given by[23, 24]

$$S_I(\omega) = 4k_\mathrm{B}T\Re\{Y(\omega)\}\frac{\hbar\omega/k_\mathrm{B}T}{\exp(\hbar\omega/k_\mathrm{B}T)-1},\qquad(4.1)$$

where $Y(\omega)$ is the complex admittance that represents the conductor's linear response. $Y(\omega)$ is a frequency-dependent, complex quantity, and reactive elements such as magnetic self-inductance and capacitance (either electrostatic or quantum) can in general affect the

noise current spectrum [25]. However, even in the most intrinsic case (i.e., after excluding these parasitic reactive elements), $Y(\omega)$ must still be frequency-dependent, because the current response to an applied voltage entails not only the electron scattering (resulting in a ohmic resistance R) but also the collective inertial acceleration of electrons, which manifests as a kinetic inductance L_K **[26].** For a conductor with an arbitrary single-electron energy dispersion $\varepsilon(\mathbf{k})$, L_K can be obtained by calculating the ac conductivity or dielectric function within the linear response framework [1, 27, 28]. In particular, the semi-classical approximation yields [1, 28]

$$
L_K = \frac{l}{W} \frac{\hbar^2}{ge^2} \left[\iint \frac{d^d\mathbf{k}}{(2\pi)^d} \frac{\partial^2 \varepsilon}{\partial k_x^2} f(\varepsilon(\mathbf{k})) \right]^{-1},
\tag{4.2}
$$

for a conductor with length l along x-axis—along which $Y(\omega)$ and $S_I(\omega)$ are measured—and cross-sectional width or area W depending on conductor dimension $d = 2$ or 3. g accounts for degeneracy (*e.g.*, due to spin and valley) and $f(\varepsilon) = [1 + \exp\{(\varepsilon - \mu)/(k_B T)\}]^{-1}$ is Fermi-Dirac distribution (μ: chemical potential). Then

$$
Y(\omega) = (R + i\omega L_K)^{-1},
\tag{4.3}
$$

with L_K and R in series. The corresponding circuit model is in Fig. 4.1(a). At low frequencies, Eq. (4.1) reduces to the familiar $4k_B T/R$. In the classical regime ($\hbar \to 0$), Eq. (4.1) reduces to

$$
S_I(\omega) = 4k_B T \Re\{Y(\omega)\}.
\tag{4.4}
$$

Integrating Eq. (4.4) over the frequency yields

$$\langle I^2 \rangle = \int_0^\infty S_I(\omega) \frac{d\omega}{2\pi} = \frac{k_B T}{L_K}. \tag{4.5}$$

In other words, in the classical regime, the current noise follows the equipartition theorem, storing a mean thermal energy of $k_B T/2$ into the collective degree of freedom associated with L_K.

So in principle the collective inertial effect L_K must influence the thermal noise spectrum. But little attention has been paid to this effect, as it is not too conspicuous—if not negligible—in most traditional conductors. To see this, note that the Planck factor in Eq. (4.1) rolls off with frequency with a characteristic cutoff $\omega_q \equiv k_B T/\hbar$, while $\Re\{Y(\omega)\}$ rolls off with a characteristic cutoff $\omega_p \equiv R/L_K = \tau^{-1}$ (τ: electron momentum relaxation time), where $R/L_K = \tau^{-1}$ is from the semiclassical calculation of the ac conductivity[1]. In traditional conductors, ω_q tends to be smaller than, or at best comparable to, ω_p across a broad temperature range, rendering the L_K effect masked in the spectrum. **Furthermore, L_K is usually smaller than the usual magnetic self-inductance L_m. However, in recently advanced nanoscale or low-dimensional conductors such as graphene, τ is large enough that $\omega_p \ll \omega_q$ and $L_K \gg L_m$ is possible[29, 28], in which case the L_K effect will dominate the spectrum roll-off.**

The purpose of work is to highlight this collective inertial effect on thermal noise spectrum from both fundamental microscopic and practical modeling points of view. In Sec. 4.2, we will delineate the effect from a microscopic standpoint. The collective excitation of electrons, macroscopically represented by L_K, exhibits a well-defined collective mass [30, 28, 26]. Since its acceleration is essential for propagating the plasmonic

wave[31, 19, 2, 26, 28, 32, 18], we will call this collective mass, normalized to the number of electrons, as plasmonic mass m_p. We will elucidate that the correct mass to use in describing the microscopic dynamics of thermal fluctuation is not the single-electron effective mass m^* but the plasmonic mass m_p. In fact, this essential link between m_p (or L_K) and thermal noise is subsumed by, and thus a natural consequence of, the linear response theory; *i.e.*, both the fluctuation-dissipation theorem and m_p are attained from the same linear response framework applied to the collection of electrons [23, 24]. In Sec. 4.3, we will elaborate on how the plasmonic roll off can take over the Planck (quantum) roll off in the noise spectrum for large enough τ. Section 4.4 will use graphene as an example conductor and develop its thermal noise model, considering the plasmonic mass effect from both electron and hole bands that co-exist.

4.2   Collective Mode & Noise: Microscopic View

4.2.1   Plasmonic Mass

We first detail the concept of plasmonic mass [28] that is paramount in this paper. If we collectively displace each electron in a conductor—*e.g.*, by applying an electric field and setting a current—by δ in the k_x direction, the total energy of the electron system is increased. The *increase amount* is the collective kinetic energy E_K corresponding to the

current; it is given by

$$E_{\mathrm{K}} \; = \; Wl \iint \frac{d^d\mathbf{k}}{(2\pi)^d} g\varepsilon(\mathbf{k}+\delta\hat{\mathbf{k}}_x) f(\varepsilon(\mathbf{k}))$$
$$-Wl \iint \frac{d^d\mathbf{k}}{(2\pi)^d} g\varepsilon(\mathbf{k}) f(\varepsilon(\mathbf{k})), \tag{4.6}$$

where the integration is over the conduction band—up to Sec. 4.3, we focus on a conductor with a single conduction band—and $\hat{\mathbf{k}}_x$ is a unit vector along the k_x axis. For a small enough δ which is practically always the case, we can write Eq. (4.6) in powers of δ

$$E_{\mathrm{K}} \; = \; \delta \times Wlg \iint \frac{d^d\mathbf{k}}{(2\pi)^d} \frac{\partial\varepsilon}{\partial k_x} f(\varepsilon(\mathbf{k}))$$
$$+\frac{\delta^2}{2} \times Wlg \iint \frac{d^d\mathbf{k}}{(2\pi)^d} \frac{\partial^2\varepsilon}{\partial k_x^2} f(\varepsilon(\mathbf{k})) + ... \tag{4.7}$$

If we assume inversion symmetry, $\varepsilon(\mathbf{k}) = \varepsilon(-\mathbf{k})$, met by many lattice types, the first term vanishes. But more broadly, since the first term is proportional to the integration of the group velocity, $v_x(\mathbf{k}) = (1/\hbar)(\partial\varepsilon/\partial k_x)$, weighted by the Fermi-Dirac distribution, if it did not vanish, there would be a spontaneous current; we do not consider such a case here, and set the first term to zero. Now, as δ and collective crystal momentum P are related by $P = nWl \times \hbar\delta$—here, $n = \iint (d^d\mathbf{k}/(2\pi)^d) g f(\varepsilon(\mathbf{k}))$ is electron number density per area or volume ($d = 2$ or 3)—, Eq. (4.7) becomes

$$E_{\mathrm{K}} \; = \; \frac{P^2}{2} \times \frac{g}{\hbar^2 n^2 Wl} \iint \frac{d^d\mathbf{k}}{(2\pi)^d} \frac{\partial^2\varepsilon}{\partial k_x^2} f(\varepsilon(\mathbf{k})). \tag{4.8}$$

So $E_K \propto \delta^2 \propto P^2$ regardless of $\varepsilon(\mathbf{k})$. This quadratic relation is expected as E_K is minimum at $\delta = 0$ (whether electrons move to right or left, E_K increases). As $E_K \propto P^2$ is Newtonian, the collective inertia is

$$M = \frac{P^2}{2E_K} = \frac{\hbar^2 n^2 W l}{g} \left[\iint \frac{d^d\mathbf{k}}{(2\pi)^d} \frac{\partial^2 \varepsilon}{\partial k_x^2} f(\varepsilon(\mathbf{k})) \right]^{-1}. \tag{4.9}$$

Collective mass per electron—plasmonic mass—is then

$$m_\mathrm{p} = \frac{\hbar^2 n}{g} \left[\iint \frac{d^d\mathbf{k}}{(2\pi)^d} \frac{\partial^2 \varepsilon}{\partial k_x^2} f(\varepsilon(\mathbf{k})) \right]^{-1} \tag{4.10}$$

which is the harmonic mean of the effective mass tensor component $\hbar^2 \left[\mathbf{M}^{-1}(\mathbf{k}) \right]_{xx} = \partial^2 \varepsilon / \partial k_x^2$. For later use, we re-express Eq. (4.10) after integration by parts:

$$m_\mathrm{p} = \frac{n}{g} \left[\iint \frac{d^d\mathbf{k}}{(2\pi)^d} v_x^2(\mathbf{k}) \left(-\frac{\partial f}{\partial \varepsilon} \right) \right]^{-1}. \tag{4.11}$$

We now make a few key observations about m_p.

Plasmonic Mass vs Effective Mass For a general $\varepsilon(\mathbf{k})$, m_p differs from the single-electron effective mass, $m^* = [1/\hbar^2 \times \partial^2 \varepsilon(\mathbf{k})/\partial k_x^2]^{-1}$. m_p is $\mathbf{k}$-independent, while m^* is generally $\mathbf{k}$-dependent. m_p generally varies with T and n, for it arises from the collective excitation, while m^* does not. In the special case of $\varepsilon(\mathbf{k}) \propto k^2$ ($k \equiv |\mathbf{k}|$), m^* is a well-defined, $\mathbf{k}$-independent constant and $m^* = m_\mathrm{p}$, as seen from Eq. (4.10) in connection with $n = \iint (d^d\mathbf{k}/(2\pi)^d) g f(\varepsilon(\mathbf{k}))$.

Plasmonic Mass vs Cyclotron Mass Consider a 2D conductor at $T = 0$ with an isotropic single-electron dispersion, $\varepsilon(\mathbf{k}) = \varepsilon(k)$. Integrations in Eq. (4.10) and $n = \iint (d^2\mathbf{k}/4\pi^2) g f(\varepsilon(\mathbf{k}))$ for $|\mathbf{k}| \leq k_F$ yield $m_p(T = 0) = \hbar^2 k_F (dk/d\varepsilon)_{k=k_F}$ (k_F: Fermi wavenumber). On the other hand, the cyclotron mass for electrons that orbit around the Fermi surface enclosing the $\mathbf{k}$-space area of $A(\varepsilon)$ is $m_c = \hbar^2/(2\pi) [(d/d\varepsilon)A(\varepsilon)]_{\varepsilon=\varepsilon_F}$ [1, 33], which, for isotropic 2D conductors, is

$$m_c = \frac{\hbar^2}{2\pi} \left[\frac{dk}{d\varepsilon} \cdot \frac{d(\pi k^2)}{dk} \right]_{k=k_F} = \hbar^2 k_F \left(\frac{dk}{d\varepsilon} \right)_{k=k_F}. \tag{4.12}$$

Thus, for a 2D isotropic conductor, $m_p(T = 0) = m_c$. This also applies to 3D conductors with $\varepsilon(\mathbf{k}) = \varepsilon(k)$.

Plasmonic Mass vs Kinetic Inductance The current due to the collective shift of electrons is an integral over the *perturbed* group velocity, $v_x(\mathbf{k} + \delta\hat{\mathbf{k}}_x)$:

$$I = W \iint \frac{d^d\mathbf{k}}{(2\pi)^d} g e v_x(\mathbf{k} + \delta\hat{\mathbf{k}}_x) f(\varepsilon(\mathbf{k})), \tag{4.13}$$

which, to the first order of δ, is

$$I = \delta \times \frac{Wge}{\hbar} \iint \frac{d^d\mathbf{k}}{(2\pi)^d} \frac{\partial^2\varepsilon}{\partial k_x^2} f(\varepsilon(\mathbf{k})). \tag{4.14}$$

Thus $E_K \propto \delta^2 \propto I^2$, and we identify the constant of proportionality as $L_K/2 = E_K/I^2$. Using Eqs. (4.8) and (4.14), we have:

$$L_K = \frac{l}{W}\frac{\hbar^2}{ge^2}\left[\iint \frac{d^d\mathbf{k}}{(2\pi)^d}\frac{\partial^2\varepsilon}{\partial k_x^2}f(\varepsilon(\mathbf{k}))\right]^{-1}. \qquad (4.15)$$

This is identical to Eq. (4.2) obtained from the semiclassical calculation of the ac conductivity [1]. Finally, from Eq. (4.10) and Eq. (4.15), we obtain

$$L_K = \frac{l}{W}\frac{m_p}{ne^2}. \qquad (4.16)$$

This establishes the link between macroscopic L_K and microscopic m_p. Eq. (4.16) is the generalization of the more familiar expression for L_K derived from the Drude model for the special case of $\varepsilon(\mathbf{k}) \propto k^2$ and $m_p = m^*$.

4.2.2 Graphene as example

While $m^* = 0$, $m_p \neq 0$. As graphene is isotropic with $\varepsilon(\mathbf{k}) = \hbar v_F k$, $m_p(T=0) = m_c = \varepsilon_F/v_F^2$ like the rest mass in relativity (ε_F and v_F are Fermi energy and velocity). m_c was measured from Shubnikov-de Haas oscillations [34, 35]. m_p was hinted at from the measured plasmonic dispersion [11, 8], and was recently directly measured by accelerating it with a microwave field [28]. In this measurement, the sample was found to have a kinetic inductance three orders of magnitude larger than the magnetic inductance.

4.2.3 From Macroscopic to Microscopic Picture

We established the macroscopic energy equipartition in the classical regime, Eq. (4.5); the noise current I stores a thermal energy of $k_B T/2$ into L_K. We now convert this macroscopic energy equipartition to a microscopic form applicable to the thermal fluctuation velocity v_{fl}—along the x-axis where noise is measured—for an individual electron. As each electron contributes a fluctuating current of $v_{fl} e/l$, $\langle I^2 \rangle = \langle v_{fl}^2 \rangle e^2/l^2 \times nWl$. By combining this with Eq. (4.5) and Eq. (4.16), we obtain

$$\langle v_{fl}^2 \rangle = \frac{k_B T}{m_p}, \tag{4.17}$$

which holds for arbitrary $\varepsilon(\mathbf{k})$. While the thermal motions of electrons are not apparently collective, the fluctuating velocity stores a thermal energy of $k_B T/2$ into the plasmonic mass m_p—as opposed to the single-electron effective mass m^*—with the plasmonic motion being an appropriate degree of freedom to apply the energy equipartition to at the microscopic level. We emphasize that the energy equipartition does not apply generally to m^*, *i.e.*, $\langle v_{fl}^2 \rangle \neq k_B T/m^*$, in general. While $\langle v_{fl}^2 \rangle = k_B T/m^*$ is valid when $\varepsilon(\mathbf{k}) \propto k^2$ and $m^* = m_p$, it faces a problem for a general, non-parabolic $\varepsilon(\mathbf{k})$, where m^* is dependent on $\mathbf{k}$. A more dramatic example where $\langle v_{fl}^2 \rangle = k_B T/m^*$ fails is the case of graphene, where $m^* = 0$. In sum, the proper mass to use in describing thermal noise dynamics is not m^* but m_p. In the time-domain description, the Langevin equation [23] should use m_p, not m^*.

4.2.4 From Microscopic to Macroscopic Picture

The foregoing discussion started by integrating the power spectral density of Eq. (4.4) into the macroscopic equipartition of Eq. (4.5) and subsequently obtained the microscopic equipartition of Eq. (4.17). We may reverse this chain of processes, and derive first the microscopic equipartition by enumerating and averaging the effect of each individual electron based on the Fermi-Dirac statistics.

To this end, for a **k**-state, we define a unitless random variable $s_\mathbf{k}$, which assumes a value of 1 with probability $f(\varepsilon(\mathbf{k}))$ and a value of 0 with probability $1 - f(\varepsilon(\mathbf{k}))$. That is, $s_\mathbf{k} = 1$ means that the **k**-state is occupied by an electron, while $s_\mathbf{k} = 0$ signifies the emptiness of the **k**-state. Then, the sum of the x-component group velocities of all electrons in the conductor can be written as

$$v_{\text{sum}} = \sum_\mathbf{k} v_x(\mathbf{k})s_\mathbf{k}, \tag{4.18}$$

which itself is a random variable. Its variance, which represents the fluctuation in the velocity sum, must be related to the above-discussed $\langle v_{\text{fl}}^2 \rangle$ by:

$$nWl \times \langle v_{\text{fl}}^2 \rangle = \langle v_{\text{sum}}^2 \rangle - \langle v_{\text{sum}} \rangle^2. \tag{4.19}$$

We evaluate each term on the right hand side by using Eq. (4.18). The first term is

$$
\begin{aligned}
\langle v_{\text{sum}}^2 \rangle &= \left\langle \left(\sum_{\mathbf{k}} v_x(\mathbf{k}) s_{\mathbf{k}} \right)^2 \right\rangle \\
&= \sum_{\mathbf{k}} v_x^2(\mathbf{k}) \langle s_{\mathbf{k}}^2 \rangle + \sum_{\mathbf{k} \neq \mathbf{k}'} v_x(\mathbf{k}) v_x(\mathbf{k}') \langle s_{\mathbf{k}} s_{\mathbf{k}'} \rangle \\
&= \sum_{\mathbf{k}} v_x^2(\mathbf{k}) f_{\mathbf{k}} + \sum_{\mathbf{k} \neq \mathbf{k}'} v_x(\mathbf{k}) v_x(\mathbf{k}') f_{\mathbf{k}} f_{\mathbf{k}'},
\end{aligned}
$$

where $f_{\mathbf{k}}$ is a shorthand notation for $f(\varepsilon(\mathbf{k}))$, and we have used $\langle s_{\mathbf{k}} s_{\mathbf{k}'} \rangle = \langle s_{\mathbf{k}} \rangle \langle s_{\mathbf{k}'} \rangle$ for $\mathbf{k} \neq \mathbf{k}'$, $\langle s_{\mathbf{k}} \rangle = 1 \cdot f_{\mathbf{k}} + 0 \cdot (1 - f_{\mathbf{k}}) = f_{\mathbf{k}}$, and $\langle s_{\mathbf{k}}^2 \rangle = 1^2 \cdot f_{\mathbf{k}} + 0^2 \cdot (1 - f_{\mathbf{k}}) = f_{\mathbf{k}}$. Similarly,

$$
\begin{aligned}
\langle v_{\text{sum}} \rangle^2 &= \left(\sum_{\mathbf{k}} v_x(\mathbf{k}) \langle s_{\mathbf{k}} \rangle \right)^2 \\
&= \sum_{\mathbf{k}} v_x^2(\mathbf{k}) f_{\mathbf{k}}^2 + \sum_{\mathbf{k} \neq \mathbf{k}'} v_x(\mathbf{k}) v_x(\mathbf{k}') f_{\mathbf{k}} f_{\mathbf{k}'}.
\end{aligned}
$$

By plugging these two results into Eq. (4.19), we obtain

$$
\langle v_{\text{fl}}^2 \rangle = \frac{1}{nWl} \sum_{\mathbf{k}} v_x^2(\mathbf{k}) f_{\mathbf{k}} (1 - f_{\mathbf{k}}). \tag{4.20}
$$

In the special case where there is inversion symmetry in the single-electron energy dispersion, i.e., $\varepsilon(\mathbf{k}) = \varepsilon(-\mathbf{k})$ and $v_x(\mathbf{k}) = -v_x(-\mathbf{k})$, Eq. (4.20) has a particularly simple interpretation. In this case, if a $\mathbf{k}$-state and a $-\mathbf{k}$-state are both occupied, the group velocities of the two occupant electrons cancel each other due to the symmetry, not contributing to the fluctuation. Thus to evaluate $\langle v_{\text{fl}}^2 \rangle$ in this special case, one has to enumerate only those situations where $\mathbf{k}$-state is occupied while $-\mathbf{k}$-state is not. The corresponding probability is then $f_{\mathbf{k}} (1 - f_{-\mathbf{k}}) = f_{\mathbf{k}} (1 - f_{\mathbf{k}})$, and hence Eq. (4.20). However, in attaining Eq.

(4.20), we have not imposed any condition on $\varepsilon(\mathbf{k})$—such as the inversion symmetry—, and hence, Eq. (4.20) is generally valid.

Converting Eq. (4.20) into an integral and using $f(\varepsilon(\mathbf{k}))[1 - f(\varepsilon(\mathbf{k}))] = -k_{\mathrm{B}}T(\partial f / \partial \varepsilon)$, we obtain

$$
\begin{aligned}
\langle v_{\mathrm{fl}}^2 \rangle &= \frac{1}{n} \iint \frac{d^d\mathbf{k}}{(2\pi)^d} g v_x^2(\mathbf{k}) f(\varepsilon(\mathbf{k}))[1 - f(\varepsilon(-\mathbf{k}))] \\
&= \frac{g k_{\mathrm{B}}T}{n} \iint \frac{d^d\mathbf{k}}{(2\pi)^d} v_x^2(\mathbf{k}) \left(-\frac{\partial f}{\partial \varepsilon} \right) \\
&= \frac{k_{\mathrm{B}}T}{m_{\mathrm{p}}},
\end{aligned}
\tag{4.21}
$$

where we have taken the last step by using Eq. (4.11). As seen, the microscopic equipartition with m_{p} resurfaces but this time via the *ab initio* calculation, which reaffirms the critical relevance of m_{p} to noise dynamics.

Eq. (4.16) with $\langle I^2 \rangle = \langle v_{\mathrm{fl}}^2 \rangle e^2 / l^2 \times nWl$ transforms this microscopic equipartition into the macroscopic equipartition, Eq. (4.5). We can subsequently work out the noise power spectral density: as $\langle I(0)I(t) \rangle = \langle I^2 \rangle e^{-|t|/\tau}$ [23], $S_I(\omega) = 4 \int_0^\infty dt \, \langle I(0)I(t) \rangle \cos(\omega t) = 4\langle I^2 \rangle \times \tau/(1 + \omega^2\tau^2)$; by using Eq. (4.5) and $\tau = L_{\mathrm{k}}/R$, we obtain the noise power spectral density of Eq. (4.4).

The power spectral density derivation above tacitly assumed frequency-independent τ and R. But even when τ and R are frequency dependent, we can still derive the power spectral density from the microscopic equipartition $\langle v_{\mathrm{fl}}^2 \rangle = k_{\mathrm{B}}T/m_{\mathrm{p}}$ by using the generalized Langevin equation of Kubo's linear response theory [23], where (and importantly) m_{p} is to be used instead of m^*.

4.3 High-Frequency Behavior of $S_I(\omega)$

With $Y(\omega) = (R + i\omega L_{\mathrm{K}})^{-1}$, Eq. (4.1) is written out as

$$S_I(\omega) = 4k_{\mathrm{B}}T \cdot \frac{R}{R^2 + \omega^2 L_{\mathrm{K}}^2} \cdot \frac{\hbar\omega/k_{\mathrm{B}}T}{\exp(\hbar\omega/k_{\mathrm{B}}T) - 1}. \tag{4.22}$$

The second factor is $\Re\{Y(\omega)\}$ and the third Planck factor is due to the radiation quantization. With frequency, the Planck factor starts rolling off at around the 'quantum cutoff', $\omega_{\mathrm{q}} = k_{\mathrm{B}}T/\hbar$; at $T = 300$ K, $\omega_{\mathrm{q}}/(2\pi) \sim 6.25$ THz. On the other hand, $\Re\{Y(\omega)\}$ starts rolling off at around the 'plasmonic cutoff', $\omega_{\mathrm{p}} = R/L_{\mathrm{K}} = 1/\tau$. In most typical conductors with τ between $\sim 10^{-14}$ s and $\sim 10^{-16}$ s, ω_{p} tends to be larger than, or at best comparable to, ω_{q}. So the noise spectrum roll-off due to L_{K} (or m_{p}) is typically masked (or at best blurred) by that due to the Planck factor.

By contrast, recent advances in nanoscale or low-dimensional conductors such as graphene have greatly increased τ so that $\omega_{\mathrm{p}} \ll \omega_{\mathrm{q}}$ is possible[29, 28], with which $Y(\omega)$ becomes substantially inductive at GHz to THz frequencies and the spectrum roll-off due to L_{K} kicks in before the Planck factor suppresses the spectrum. To show this concretely, Fig. 4.1(b) plots Eq. (4.22)—noise spectrum *vs.* frequency—for various values of τ. For $\tau = 0$ (black curve), the noise spectrum starts decreasing around at ω_{q}; this is the noise suppression due purely to the Planck factor. As τ is increased and ω_{p} becomes increasingly smaller than ω_{q}, the high-frequency suppression of the noise spectrum becomes increasingly dominated by the L_{K} effect; compare the blue, green, and red curves—τ increasing in that order—against the black curve. For such large τ values, the L_{K} effect on
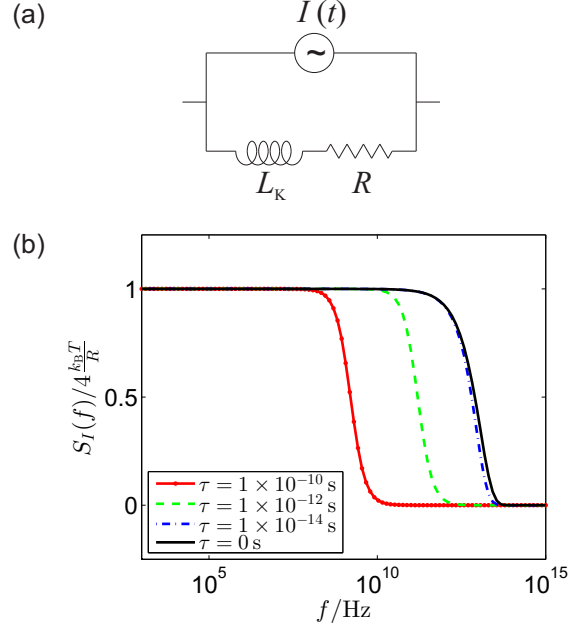
Figure 4.1: **a.** Circuit model for the Johnson-Nyquist noise, including the kinetic inductance effect. **b.** Current noise power spectral density for various τ values at $T = 300$ K.

thermal noise is critical to model in. This effect may also be exploited to infer the optical

(plasmonic) properties from the noise spectrum.

To further highlight the critical role of L_K in the noise spectrum for large τ, we compute

$\langle I^2 \rangle$ by integrating Eq. (4.22) across the entire frequency:

$$\langle I^2 \rangle = \frac{k_B T}{L_k} \times \frac{2}{\pi} \int_0^\infty \frac{a}{a^2 + x^2} \frac{x dx}{e^x - 1} \tag{4.23}$$

where $a \equiv \omega_p/\omega_q = R\hbar/(k_B T L_K) = \hbar/(k_B T \tau)$ and $x \equiv \hbar\omega/(k_B T)$. This generalizes Eq.

(4.5) by including the Planck quantization. $\langle I^2 \rangle$ *vs.* a is in Fig. 4.2. For $a \to \infty$ ($\tau \to 0$;

$\omega_p \gg \omega_q$), the Planck quantization effect takes precedence over the L_K effect, and $\langle I^2 \rangle \ll$
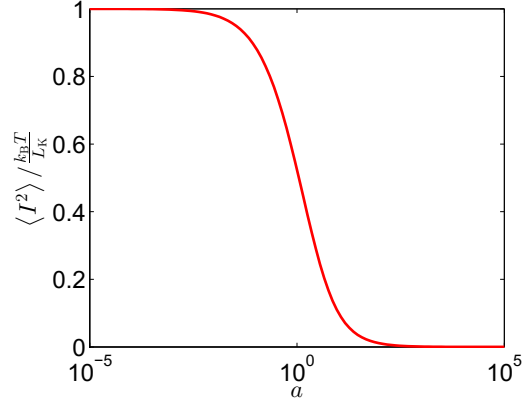
Figure 4.2: $\langle I^2 \rangle$ normalized to $k_B T/L_K$ *vs.* $a \equiv \omega_p/\omega_q$.

$k_B T/L_K$. In fact, in this case, Eq. (4.23) is reduced to

$$\langle I^2 \rangle = \frac{k_B T}{L_K} \times \frac{2}{\pi a} \int_0^\infty \frac{x dx}{e^x - 1} = \frac{\pi (k_B T)^2}{3 R \hbar} \tag{4.24}$$

where L_K disappears. In contrast, for $a \to 0$ ($\tau \to \infty$; $\omega_p \ll \omega_q$), we have

$$\langle I^2 \rangle = \frac{k_B T}{L_K} \times \frac{2a}{\pi} \int_0^\infty \frac{1}{a^2 + x^2} dx = \frac{k_B T}{L_K}, \tag{4.25}$$

recovering the macroscopic equipartition, Eq. (4.5). *I.e.*, in this case, the spectrum roll-off is entirely governed by L_K with the Planck quantization effect masked.

4.4 Thermal Noise Model for Graphene

Graphene is an ideal system to apply the foregoing formalism to and to derive a thermal noise model from for a few reasons. First, in high-quality graphene, $\tau \sim 10^{-12}$ s [29,

28], corresponding to the green curve of Fig. 4.1(b), and hence, the effect of L_K (or m_p) dominates over the Planck quantization effect in the noise spectrum. Second, in graphene, $m^* = 0$ yet $m_p \neq 0$, and hence m_p varies with n and T, enriching the noise behaviors (in contrast, in conductors with $\varepsilon(\mathbf{k}) \propto k^2$ and $m_p = m^* \neq 0$, m_p is independent of n and T). Third, since in graphene both conduction and valence bands contribute to electronic conduction, L_K (or m_p) from both bands should be considered, which further complicates the noise behaviors.

First consider a fictitious graphene with only conduction band, held at a constant charge density by a gate bias. With only the electron band, the constant charge density means a constant electron number density n. Suppose $\mu(T=0) = \varepsilon_F = 0.1$ eV. With $g = 4$, $n = \int (d^2\mathbf{k}/\pi^2) f(\varepsilon(\mathbf{k}))|_{\mu=\varepsilon_F, T=0} = \varepsilon_F^2/(\pi\hbar^2 v_F^2)$. As n is T-independent in our scenario,

$$ n = \int \frac{d^2\mathbf{k}}{\pi^2} f(\varepsilon(\mathbf{k}))|_{\mu,T} = \frac{1}{\pi}\frac{\varepsilon_F^2}{\hbar^2 v_F^2}, \tag{4.26} $$

from which $\mu(T)$ is determined (Fig. 4.3(a), blue curve). Using this $\mu(T)$ in Eq. (4.10), we evaluate m_p. As n is constant, $L_K \propto m_p$ (Eq. (4.16)). Figure 4.3(b) shows L_K and m_p as functions of T; both increase with T. This contrasts the case of a conventional conductor with parabolic dispersion, for which m_p (and L_K with the fixed n with the gate biasing) is independent of T.

A real graphene sample where electron and hole bands co-exist exhibit even richer behaviors. We again assume a constant charge density held by a gate bias and suppose $\mu(T=0) = \varepsilon_F = 0.1$ eV. At $T = 0$, graphene is electron-doped. As T rises, both the electron number density n_e and hole number density n_h—subscript 'e' and 'h' signify
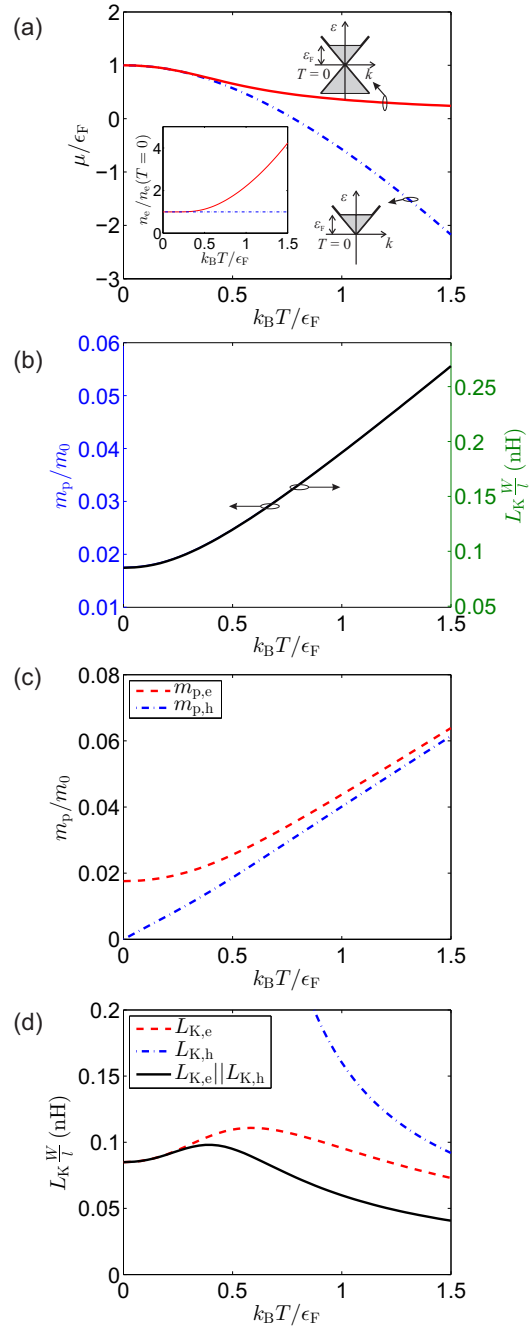
Figure 4.3: **a.** $\mu(T)$ for fictitious graphene (blue curve) and real graphene (red curve), shown with electronic band structures. $\varepsilon_F = 0.1$ eV for both. Inset: n_e for both systems. **b.** m_p, L_K *vs.* T for fictitious graphene. m_0 is intrinsic electron mass. **c.** m_p in each band *vs.* T for real graphene. **d.** L_K in each band *vs.* T for real graphene. $L_{K,e} || L_{K,h}$ is also shown.

electron and hole bands—can vary (this contrasts the fictitious case where the electron number density is fixed) while the total charge density $-en_{\mathrm{e}} + en_{\mathrm{h}}$ is fixed. Formally:

$$n_{\mathrm{e}}(\mu, T) - n_{\mathrm{h}}(\mu, T) = \frac{1}{\pi} \frac{\varepsilon_{\mathrm{F}}^2}{\hbar^2 v_{\mathrm{F}}^2}, \tag{4.27}$$

where

$$n_{\mathrm{e}}(\mu, T) = \int_{\mathrm{e}} \frac{d^2 \mathbf{k}}{\pi^2} f(\varepsilon(\mathbf{k}))|_{\mu, T}, \tag{4.28}$$

$$n_{\mathrm{h}}(\mu, T) = \int_{\mathrm{h}} \frac{d^2 \mathbf{k}}{\pi^2} \left[1 - f(\varepsilon(\mathbf{k}))|_{\mu, T} \right]. \tag{4.29}$$

This leads to a markedly different behavior for $\mu(T)$ with $\mu \to 0$ for $T \to \infty$ (Fig. 4.3(a), red curve), as compared to the case of the fictitious graphene (Fig. 4.3(a), blue curve). Once $\mu(T)$ is evaluated, $n_{\mathrm{e}}(T)$ and $n_{\mathrm{h}}(T)$ follow from Eqs. (4.28) and (4.29). Also with $\mu(T)$, we can evaluate $m_{\mathrm{p,e}}$ and $m_{\mathrm{p,e}}$,

$$m_{\mathrm{p,e}} = \frac{\hbar^2 n_{\mathrm{e}}}{g} \left[\iint_{\mathrm{e}} \frac{d^d \mathbf{k}}{(2\pi)^d} \frac{\partial^2 \varepsilon}{\partial k_x^2} f(\varepsilon(\mathbf{k}))|_{\mu, T} \right]^{-1}, \tag{4.30}$$

$$m_{\mathrm{p,h}} = \frac{\hbar^2 n_{\mathrm{h}}}{g} \left[\iint_{\mathrm{h}} \frac{d^d \mathbf{k}}{(2\pi)^d} \frac{\partial^2 \varepsilon}{\partial k_x^2} \left[1 - f(\varepsilon(\mathbf{k}))|_{\mu, T} \right] \right]^{-1}, \tag{4.31}$$

which are variations of Eq. (4.10). Finally, using the results above in Eq. (4.16), we can compute the kinetic inductance L_{K} of each band separately.

Figures 4.3(c) and (d) plot the resulting m_{p} and L_{K} in each band as functions of T. They again exhibit conspicuous T dependency just like in the fictitious case. However, the T-dependency of $L_{\mathrm{K,e}}$ with a maximum value (Fig. 4.3(d)) markedly differs from the

monotonically increasing T-dependency of $L_{K,e}$ of the fictitious case (Fig. 4.3(b)). $L_{K,e} \sim$ $m_{p,e}/n_e$ (Eq. (4.16)) exhibits the maximum value in the real graphene due to competing effects of $m_{p,e}$ and n_e. For small T, $n_h \ll n_e \approx$ constant so $L_{K,e}$ increases with T as $m_{p,e}$ increases with T. This is just like in the fictitious case. In contrast, for large T, n_e grows as T^2 (as does n_h to keep the overall charge density constant), which is faster than the growth of $m_{p,e}$ with T (compare Fig. 4.3(a) inset and Fig. 4.3(c)); therefore, $L_{K,e} \sim m_{p,e}/n_e$ decreases for large T.
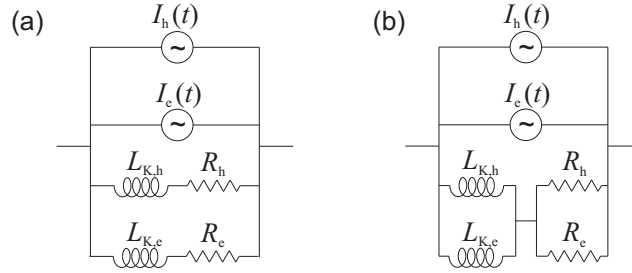
Figure 4.4: **a.** Circuit noise model for graphene. **b.** For $\tau_e = \tau_h$.

The circuit noise model of the real graphene is shown in Fig. 4.4(a), where the L_K effect from both bands is explicitly modeled in. The total power spectral density of the current noise is given by

$$
\begin{aligned}
S_I(\omega) \;=\; & 4k_B T \left[\frac{R_e}{R_e^2 + \omega^2 L_{K,e}^2} + \frac{R_h}{R_h^2 + \omega^2 L_{K,h}^2} \right] \\
& \times \frac{\hbar\omega/k_B T}{\exp\left(\hbar\omega/k_B T\right) - 1}
\end{aligned}
\tag{4.32}
$$

assuming no correlation between the electron band noise and hole band noise. Due to the dominance of $L_{K,e}$ and $L_{K,h}$ in spectrum roll-off over the Planck quantization effect (in high-quality graphene) and due also to the rich T-dependencies of $L_{K,e}$ and $L_{K,h}$, the

noise power spectral density in graphene exhibits very different characteristics from that in traditional conductors in terms of both frequency and temperature dependency. Whether the electron and hole band noise are correlated or not is an open question; such correlation, if extant and conspicuous, would further enrich the noise spectrum. Also note that we have ignored inter-band transitions, because they are minimal at our frequencies of interest (up to THz) for this relatively highly doped sample.

If τ is the same for both bands, *i.e.*, if $L_{K,e}/R_e = L_{K,h}/R_h$, Eq. (4.32) is reduced to

$$
\begin{aligned}
S_I(\omega) &= 4k_B T \frac{R_e||R_h}{(R_e||R_h)^2 + \omega^2(L_{K,e}||L_{K,h})^2} \\
&\quad \times \frac{\hbar\omega/k_B T}{\exp(\hbar\omega/k_B T) - 1}
\end{aligned}
\tag{4.33}
$$

where $(R_e||R_h)^{-1} = R_e^{-1} + R_h^{-1}$ and $(L_{K,e}||L_{K,h})^{-1} = L_{K,e}^{-1} + L_{K,h}^{-1}$. That is, the circuit model of Fig. 4.4(a) can be reduced to Fig. 4.4(b) with the resistors from both bands and the kinetic inductors from both bands are each connected in parallel, with $R_e||R_h$ and $L_{K,e}||L_{K,h}$ in series serving as overall resistor and inductor. For the T-dependency of $L_{K,e}||L_{K,h}$, see Fig. 4.3(d).

In general $L_{K,e}/R_e \neq L_{K,h}/R_h$, but even in such a case, $L_{K,e}||L_{K,h}$ considered right above is still of great relevance to the noise dynamics. This is because $\langle I^2 \rangle = \langle I_e^2 \rangle + \langle I_h^2 \rangle = k_B T/L_{K,e} + k_B T/L_{K,h}$ or,

$$
\langle I^2 \rangle = \frac{k_B T}{L_{K,e}||L_{K,h}}.
\tag{4.34}
$$

That is, the total integrated current noise fluctuation follows the energy equipartition, with the mean thermal energy of $k_B T/2$ stored onto the macroscopic degree of freedom associated with $L_{K,e}||L_{K,h}$. Since this parallel inductance exhibits the T dependency as

shown in Fig. 4.3(d), $\langle I^2 \rangle$ in graphene is no longer proportional to T, which is the case with conductors with quadratic single-electron energy dispersion held with a gate bias.

4.5   Conclusion

Recent advances in low-dimensional materials have blurred the traditional boundary between photonics and electronics. A prominent example is plasmonics in 2D conductors (*e.g.*, graphene); while plasmonic excitation occurs traditionally in the realm of photonics, in 2D materials it can occur at THz and GHz frequencies, reaching into the electronics realm.

This paper offered another example that highlights such merger of photonics-electronics boundaries. Concretely, we investigated how plasmonic response (traditionally studied in photonics) can significantly alter the Johnson-Nyquist thermal noise dynamics (traditionally studied in electronics). The intrinsic connection between plasmonics and Johnson-Nyquist noise is in fact a natural consequence of the linear response theory: that is, both plasmonic properties and fluctuation-dissipation relation (of which the Johnson-Nyquist noise is a prominent example) are obtained from the same linear response framework applied to the collection of electrons. But in traditional conductors with short electron scattering times, the Planck quantization effect has masked the plasmonic effect in the noise spectrum. On the other hand, in 2D materials like graphene where electron scattering time has been greatly elongated, the plasmonic effect can take the precedence over the Planck quantization effect, significantly altering the thermal noise spectrum. We

demonstrated that this effect is not only of great importance for practical noise modeling, but it also provides an opportunity to delineate some fundamental concepts, in particular, the critical role that the plasmonic mass (as opposed to the single-electron effective mass) plays in thermal fluctuation dynamics of electrons.

Chapter 5

Nonreciprocal Plasmons

We have shown in Section 2.1 that 2DEGs that have a current applied to them and whose constituent electrons have an averaged drift velocity v_0 support plasmons that have propagation velocities

$$s = \pm \frac{\omega}{k} + v_0 \tag{5.1}$$

The plus sign corresponds to the plasmon co-propagating with the drift velocity, while the minus sign correponds to the plasmon propagating against the drift velocity. This has a very simple interpretation: from the frame that is co-propagating with same velocity v_0, the plasmon dispersion is the bare, non-drifting plasmon dispersion, and the plasmons do not 'feel' the effect of the motion of the lattice ions. Thus, in moving back to the lab frame that is fixed with zero velocity, one only needs to add the difference in velocities, which is v_0. This results in a very curious system, in which the waves propagate non-reciprocally without a magnetic field. In this case, the time-reversal symmetry is broken by the drift current instead of a magnetic response. This breaking of time-reversal symmetry could

allow for useful circuits such as isolators to be constructed using this principle, instead of having to use magnetic materials. There is also the possibility of obtaining reflection gain from such non-reciprocal plasmons, which would allow new classes of oscillators to be designed, potentially with much higher frequency cutoffs. This possibility was discussed first by Dyakonov and Shur in 1993 [36] but even now has not been conclusively shown to be feasible. This chapter first demonstrates that such nonreciprocal plasmons exist in section 5.1, and in section 5.2 the reflection gain mechanism is studied in detail. Finally, in section 5.3 we describe a measurement of graphene plasmons.

5.1 Nonreciprocal plasmons in AlGaAs/GaAs

In typical 3D conductors, the effect of the nonreciprocal plasmons entirely unnoticeable: typical drift velocities in metals (less than a m/s) are orders of magnitude smaller than the electromagnetic waves propagating in the metals, which is on the order of the speed of light ($\sim 10^8$ m/s). In order to observe this effect, we need a system where these velocities can be made as close to each other as possible. The 2D plasmon in the ultra high mobility AlGaAs/GaAs heterostructure 2DEG is an ideal candidate, because its very large kinetic inductance L_K allows microwave frequency plasmon propagation at extremely low velocities down to $c/1000 \sim 3 \times 10^5$ m/s [18]. Furthermore, the low electron density and high fields in semiconductors mean that electrons drift with very large velocities (up to the saturation velocity, $\sim 1 \times 10^5$ m/s)[1]. It is this relative similarity in magnitudes of these two velocities enables this effect to be measured. Indeed, this phenomenon has been observed before by indirect raman measurement of the 2DEG plasmons [37]. This motivates us to

attempt a direct measurement of the propagation of the ultrasubwavelength plasmons, and show that the dispersion relation is modified by the drift current following Eq. 5.1.

5.1.1 Device Structure and Fabrication

The fabrication of the samples that enabled this measurement began with our collaborators Kenneth West and Loren Pfeiffer from Princeton University who provided us with the ultra-high mobility heterostructure grown on a standard semi-insulating GaAs substrate using molecular beam epitaxy (MBE), with a 75nm $Al_{0.3}Ga_{0.7}As$ layer and 5nm GaAs cap layer above the active GaAs layer. These layers will act as the gate dielectric, with a dielectric constant of 12 and a capacitance per unit area of 0.13 μF/cm^2. After measurement and verification of the mobility (>1,000,000 cm^2/Vs) and quality of the unprocessed wafer, the subsequent microfabrication steps to obtain a measurement sample were all performed at the cleanroom at the Harvard Center for Nanoscale Systems. First, a rectangular mesa to define the 2DEG boundaries were first made using photolithography and wet-etching. Next, the contact metal alloy (6 nm Ni / 30 nm Au / 60nm Ge / 20nm Ni / 150 nm Au) was deposited two sides of the rectangular square, and thermally annealed at 460 °C to allow the formation of ohmic contacts to the underlying 2DEG. These contacts serve a dual purpose of allowing us to couple microwave signals into and out of the 2DEG, while at the same time allowing for a DC voltages (and currents) to be applied to the 2DEG.

Subsequently, the gate, microwave transmission lines and contact pads areas were defined with photolithography in a single step and finally 400nm deposited and lifted off to complete the samples and for reference, a top-down optical image of the completed sample is shown in Fig. 5.1a. The 2 ohmic contacts are connected to 2 tapered coplanar

waveguide (CPW) transmission lines to allow the sample to be probed by a 100-um pitch GSG probe. The CPW ground lines are also connected to the gate above the 2DEG so that the gate acts as a microwave ground, while the CPW signal lines are connected to each other only through the 2DEG, so that the 2DEG acts as the microwave signal line. Thus, the sample functions as a CPW coupling to a short microstrip section made from a 2DEG, coupled to another CPW. This simple structure allows it to be modeled very simply using the circuit models described in Chapter 1.

5.1.2   Measurement and analysis

The measurements were performed in a cryogenic probe station (Lakeshore TTP4), which uses liquid helium to cool the sample stage down to a temperature of 4K while support-ing stable microwave connections to test equipment. This was necessary to obtain the maximum electron mobility in the GaAs, which directly reduces the plasmonic loss due to ohmic resistance and increase the quality factor Q. The samples were contacted with two 100-um pitch GSG probes which were mounted on arms with micromanipulators to enable probing of multiple samples as well as a calibration substrate in a single cooling cycle. The signal lines were connected to a 50 GHz network analyzer (Keysight E8364A) which had internal bias tees. The bias tee DC outputs were connected to 2 Keithley 2400 sourcemeters to source and measure the DC voltage and currents passing through the de-vice. These sourcemeters apply voltages V_1 and V_2 directly to each of the 2 ohmic contacts. Since the gate of the device directly DC coupled to the CPW ground lines, the gate was al-ways held at a DC potential of 0V, and changing the bias $V_1 = V_2 \neq 0$V together allows for the 2DEG layer to be charged as the carrier and the gate acts as a parallel plate capacitor.
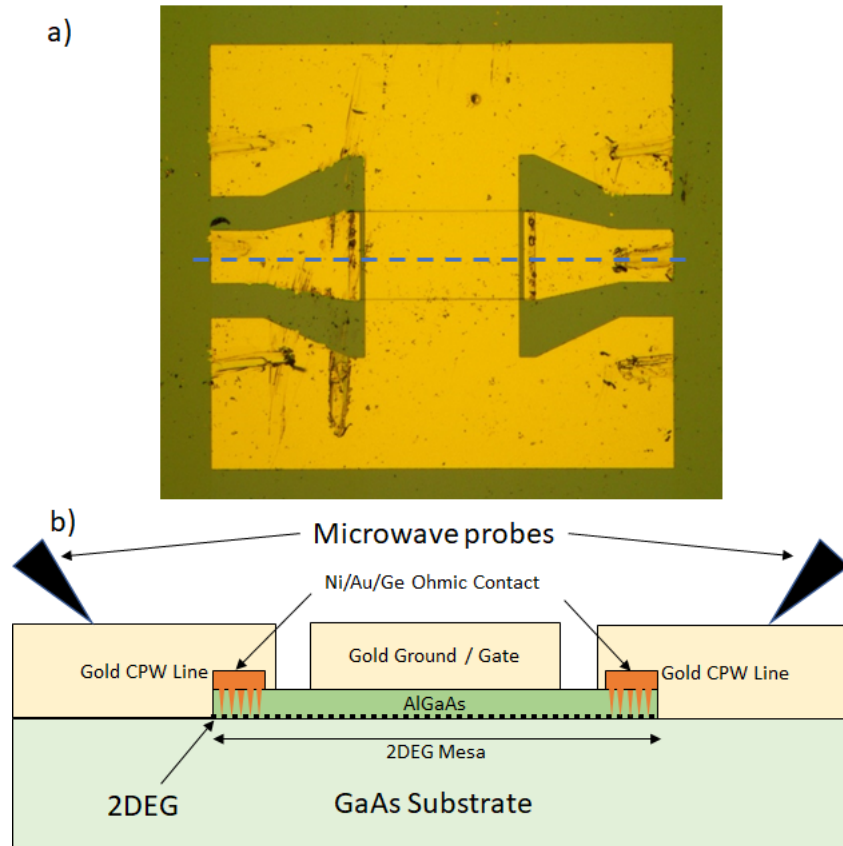
Figure 5.1: (a) Optical micrograph showing top down view of the the completed device. The yellow regions are the gold contact pads, transmission lines, and top gate. A schematic of the cross section at the blue dashed line is shown in (b). The 2DEG is denoted by the black dashed line, with its boundaries defined by a mesa 145 μm long and 85 μm wide. 5 μm wide ohmic contacts to the 2DEG were made on 2 sides of the mesa.

However, if $V_1 \neq V_2$, then a DC current flows between the ohmic contacts of the device and so the electrons in the 2DEG are set to drift. This current I is measured with each of the sourcemeters, and if the carrier density is also known, the drift velocity is easily obtained via $I = nWev$.

The microwave measurements also require very precise calibration of the network analyzer, which was performed using the multiline-TRL method using a custom calibration

substrate[38]. The calibration procedure effectively moves the measurement plane of the network analyzer from its port outputs to the probe tips, which means that a microwave measurement only includes the device s-parameters and between the probe tips, and effects from the cables, probe arms, bias tee connections, etc. are subtracted out.

The measured S-parameters as a function of frequency are shown in Fig. 5.2a. First, we note that S_{11} and S_{22} magnitudes are typically much larger than S_{12} and S_{21}, which represents much larger reflection signals than transmission signals through the 2DEG. This implies that the 2DEG is not well-matched to the 50-Ω transmission line. Even though the 2DEG characteristic impedance be tuned by changing its width, it is still not trivial to match the device to the 50-Ω line due to the ohmic contact resistance, which in my experience was very difficult to control. Small changes in the conditions of the annealing temperatures and times and cleanliness of the wafer surface resulted in ohmic contact resistances that varied greatly.
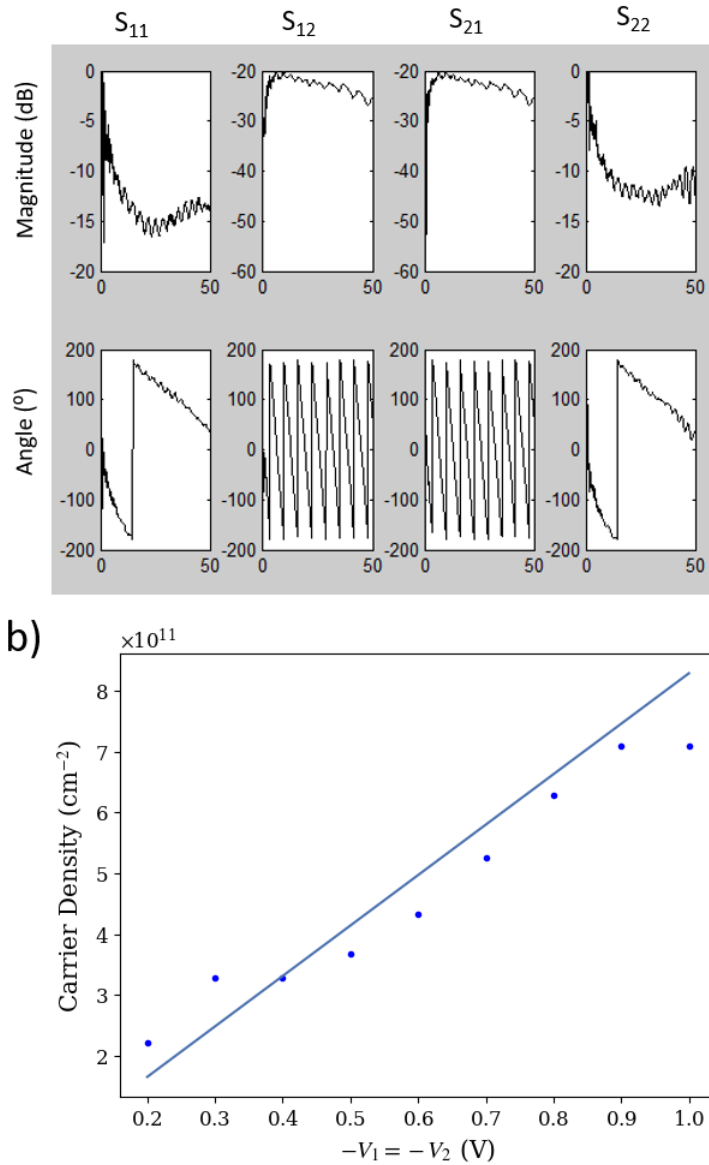
Figure 5.2: (a) Calibrated 2-port S-parameter network analyzer measurements of the device as a function of frequency from 0 to 50 GHz. The rows show the magnitude and angle of the S-parameters, while the columns are the 4 S-parameters ($S_{11}, S_{12}, S_{21}, S_{22}$) respectively. b) Carrier density of the 2DEG as a function of the applied gate voltage $-V_1 = -V_2$. The solid circles are measurements from the plasmon velocity, while the line is the expected electron density using $n = C|V_1|$

In spite of this, we could still observe clean transmission signals (See Fig. 5.2a). In particular, we note that the angle of S_{21} and S_{12} showed a very large gradient with frequency. This gradient is in fact the direct measurement of the plasmon velocity. To see this, we note that the phase delay, ϕ, as the plasmon propagates through a section of length l is

$$\phi = \arg\left(S_{12,21}\right) = -\frac{2\pi l}{\lambda} = -\frac{2\pi l}{s} f$$

with a minus sign chosen to be commensurate with the definitions of the S-parameters. Furthermore, this measurement of s also gives us a measurement of the electron density independent from the actual gate voltage applied, since $L_\mathrm{K} = \frac{1}{s^2 C}$, and L_K is directly related to the electron density (Eq. 1.4),

$$n = \frac{m_e^*}{L_\mathrm{K} e^2 W} = \frac{m_e^*}{s^2 e^2 C W}$$

. The measured n are shown in Fig. 5.2b, together with the theoretical values only using the applied voltage and capacitance $C|V_1|$. The excellent agreement between the 2 measurements demonstrates the robustness of the measurement and suggests the accuracy of the device parameters such as the capacitance and 2DEG lengths.

Next, we applied a drift current to the sample by letting varying V_1 and V_2 around an average 0.68 V. While ideally we would try to keep the electron density constant while we vary the current, this is not possible as the electron density no longer remains constant across the whole length of the 2DEG transmission line. This is because of resistive losses in the line, which necessitates a varying local potential and thus varying electron density. Thus, in practise, we vary the current by tuning V_1 and V_2 while keeping the measured

average phase velocity in the forward and backward directions, ϕ_f and ϕ_r, constant, which translates to increasing V_1 above 0.68 V while decreasing V_2, or vice-versa.
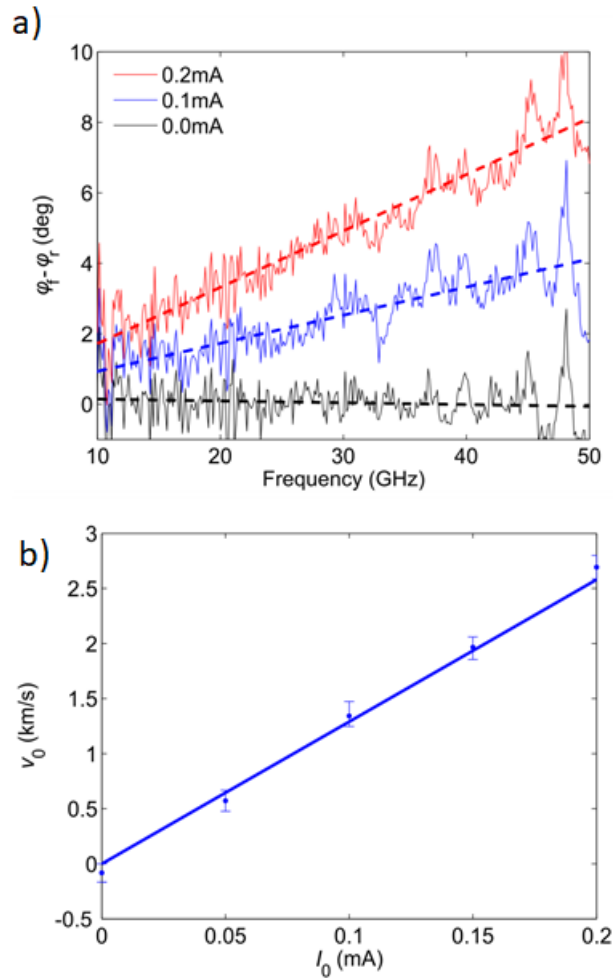
Figure 5.3: (a) Phase delay difference between the forward and backward directions as increases as current increases. b) Drift velocity extracted from the microwave phase difference $\phi_f - \phi_r$, shown as discrete data points. The error bars indicate uncertainty due to the fits required to obtain $c = s \pm v_0$. The solid line is the prediction for the drift velocity using $I = nWev$

Figure 5.3a shows the resulting measurement. One clearly sees that as current is increased, ϕ_f and ϕ_r begin to diverge from each other, and further, that this divergence increases roughly linearly with frequency. This can be understood simply by noting that for small v_0 compared with s,

$$
\begin{aligned}
\phi_f - \phi_r &= \frac{2\pi l}{s + v_0}f - \frac{2\pi l}{s - v_0}f \\
&= \frac{4\pi l}{s^2}v_0 f
\end{aligned}
$$

Thus, the slope of the graph of $\phi_f - \phi_r$ against frequency f gives a measurement of the drift velocity v_0. Therefore, fitting the measured ϕ_f and ϕ_r to a straight line to obtain the slopes allows a separate measurement of v_0 that does not require knowledge of the actual current flowing in the 2DEG, in contrast to the usual way of determining drift velocity using the equation $I = nWev$. Figure 5.3b shows the excellent agreeement between the 2 methods.

We believe that these measurements are an unequivocal demonstration of the modifications of the plasmon velocity due to drift velocity. Nevertheless, the large plasmonic losses observed suggests limitations to the possible device designs. The 2 main sources of loss are the resistive losses in the plasmons, and the losses due to the contact resistance. Further complicating this is the difficulty in separating the 2 sources of loss, since contact resistance is generally unknown until measured, and we do not have a good circuit model for the contact resistance, capacitances and inductances. Furthermore, we observed that while the largest drift velocity possible is the saturation velocity of $\sim 10^5$m/s, in practice resistive losses increases as the current and drift velocity increased. This results in a much

lower maximum current and drift velocity that can be achieved while still being able to observe plasmon propagation.

5.2 Reflection Gain from Nonreciprocal Plasmons

The experimental confirmation of the existence of nonreciprocal plasmons allows a novel method to achieve gain in an active semiconductor device. It turns out that in a 2DEG electron gas with drift, the forward and backward propagating waves not only have different speeds as described in the previous section, but also different absolute values for their wave impedances as well. At a boundary which has its load impedance fixed by the external circuit, the difference in wave impedances requires the wave amplitudes to be different. More importantly, the voltage reflection coefficient of the waves at the boundary can even be greater than 1, even from a passive, lossy load with an impedance with positive real part, which implies that the waves reflect off the load with some voltage gain. This possibility was first described in [36] by Dyakonov and Shur, who proposed utilizing this method to build an oscillator that makes use of such a gain mechanism. In this section we will study this mechanism in detail and describe attempts to measure its effect.

5.2.1 Nonreciprocal wave impedances

First, we to obtain expressions for the wave impedances, we need to write down the currents in a 2DEG including the case in which the current drifts with velocity v_0. This can be written to first order in densities ($n(x,t) = n_0 + \tilde{n}(x,t)$) and velocities ($v(x,t) = v_0 + \tilde{v}(x,t)$)

as

$$
\begin{aligned}
I(x,t) &= nWev = eW\left(\tilde{n}+n_0\right)\left(\tilde{v}+v_0\right) \\
&= eWn_0v_0 + eW\tilde{n}v_0 + eWn_0\tilde{v} \\
&= I_0 + eWv_0\frac{C}{e}\left(A_1 e^{i(k_+x+\omega t)} + A_2 e^{i(k_-x+\omega t)}\right) \\
&\quad + eAn_0\sqrt{\frac{e}{mU_0}}\left(-A_1 e^{i(k_+x+\omega t)} + A_2 e^{i(k_-x+\omega t)}\right) \\
I(x,t)-I_0 &= \left(eAv_0\frac{C}{e} - eAn_0\sqrt{\frac{e}{mU_0}}\right)A_1 e^{i(k_+x+\omega t)} \\
&\quad + \left(eAv_0\frac{C}{e} + eAn_0\sqrt{\frac{e}{mU_0}}\right)A_2 e^{i(k_-x+\omega t)}
\end{aligned}
$$

Here, we have decomposed the waves into a forward propagating part A_1 and backward propagating part A_2. We have also not included the loss terms. A more detailed calculation is possible with these terms, but it does not substantially affect the subsequent conclusions. Firstly, we might rewrite the equations in terms of $s = \sqrt{\frac{eU_0}{m}}$, which is the plasmon velocity in the case without drift, using $n_0 = \frac{CU_0}{e}$,

$$
\begin{aligned}
I(x,t)-I_0 &= \left(eAv_0\frac{C}{e} - eAn_0\frac{s}{U_0}\right)A_1 e^{i(k_+x+\omega t)} + \left(eAv_0\frac{C}{e} + eAn_0\frac{s}{U_0}\right)A_2 e^{i(k_-x+\omega t)} \\
&= AC\left(v_0 - s\right)A_1 e^{i(k_+x+\omega t)} + AC\left(v_0 + s\right)A_2 e^{i(k_-x+\omega t)}
\end{aligned}
$$

In the case of no drift the current is

$$
I = -\frac{1}{Z_0}A_1 e^{i(k_+x+\omega t)} + \frac{1}{Z_0}A_2 e^{i(k_-x+\omega t)}
$$

which reduces to the usual case for a transmission line with characteristic impedance $Z_0 = \frac{1}{ACs}$. By extension, we can identify the forward and backward wave impedances as

$$Z_\pm = \frac{1}{AC(v_0 \pm s)}$$

and crucially, has different magnitude between the forward and backward propagating waves.

This is significant because the impedance looking into the 2DEG that is terminated by some boundary is fixed by an external circuit. Suppose we have a 2DEG sample of length L from $x = -L$ to $x = 0$, terminated at the $x = 0$ end with an impedance Z_{BC}. The voltage at the end of the 2deg ($x = 0$) is given by

$$\begin{aligned} V(x = 0) &= v_+ e^{i(k_+ x + \omega t)} + v_- e^{i(k_- x + \omega t)} \\ &= v_+ + v_- \end{aligned}$$

The currents at the end are (dropping the time dependence for convenience)

$$I(x = 0) = AC\,(v_0 - s)\,v_+ + AC\,(v_0 + s)\,v_-$$

The boundary has an load (shunt) impedance of Z_{BC}, which means $V(x=0) = Z_{BC}I(x=0)$ and equivalently

$$
\begin{aligned}
v_+ + v_- &= Z_{BC}\left(AC(v_0 - s)v_+ + AC(v_0 + s)v_-\right) \\
v_+ &= \left(\frac{Z_{BC}AC(v_0 + s) - 1}{1 - Z_{BC}AC(v_0 - s)}\right)v_- \\
\Gamma \equiv \frac{v_+}{v_-} &= \left(\frac{(s + v_0) - \frac{1}{ACZ_{BC}}}{(s - v_0) + \frac{1}{ACZ_{BC}}}\right)
\end{aligned}
\tag{5.2}
$$

We can identify this as the voltage reflection coefficient. If the magnitude of Z_{BC} is large enough (which corresponds to an external open circuit), this reduces to

$$
\Gamma \equiv \frac{v_+}{v_-} \rightarrow \frac{s + v_0}{s - v_0}
$$

and thus we see that these nonreciprocal plasmons reflect off the open circuit with a voltage gain $|\Gamma| > 1$ if v_0 is positive.

Now the voltages and currents at the start of the transmission line ($x = -L$) is

$$
\begin{aligned}
V(x = -L) &= v_+ e^{-ik_+L} + v_- e^{-ik_-L} \\
I(x = -L) &= AC(v_0 - s)v_+ e^{-ik_+L} + AC(v_0 + s)v_- e^{-ik_-L}
\end{aligned}
$$

Then we have

$$
\begin{aligned}
Z_{in} &= \frac{V(x=-L)}{I(x=-L)} \\
&= \frac{v_+ e^{-ik_+ L} + v_- e^{-ik_- L}}{AC(v_0 - s)v_+ e^{-ik_+ L} + AC(v_0 + s)v_- e^{-ik_- L}} \\
&= \frac{(Z_{BC}AC(v_0+s)-1)e^{-ik_+ L} + (1-Z_{BC}AC(v_0-s))e^{-ik_- L}}{AC(v_0-s)(Z_{BC}AC(v_0+s)-1)e^{-ik_+ L} + AC(v_0+s)(1-Z_{BC}AC(v_0-s))e^{-ik_- L}}
\end{aligned}
$$

This is the most general result. Take the limit when $Z_{BC} \to \infty$,

$$
\begin{aligned}
Z_{in} &= \frac{(v_0+s)e^{-ik_+ L} - (v_0-s)e^{-ik_- L}}{(v_0-s)(AC(v_0+s))e^{-ik_+ L} + (v_0+s)(-AC(v_0-s))e^{-ik_- L}} \\
&= \frac{1}{AC(v_0^2-s^2)} \frac{v_0 e^{-ik_+ L} + s e^{-ik_+ L} - v_0 e^{-ik_- L} + s e^{-ik_- L}}{e^{-ik_+ L} - e^{-ik_- L}} \\
&= \frac{1}{AC(v_0^2-s^2)} \left(v_0 + s \frac{e^{-ik_+ L} + e^{-ik_- L}}{e^{-ik_+ L} - e^{-ik_- L}} \right) \\
&= \frac{1}{AC(v_0^2-s^2)} \left(v_0 + is \cot\left(\frac{\omega s L}{s^2 - v_0^2} \right) \right) \\
&= \frac{1}{AC(s^2-v_0^2)} \left(-v_0 - is \cot\left(\frac{\omega s L}{s^2 - v_0^2} \right) \right)
\end{aligned}
$$

When v_0 is positive, i.e. carriers are drifting into the boundary, the real part of the impedance term $\frac{-v_0}{AC(s^2-v_0^2)}$ becomes negative and appears as a gain element, at the end of the 2DEG opposite to the open circuit where the gain actually happens, and thus, the 2DEG as a whole (looking in from the $x < 0$ direction) looks like an element with gain. For comparison, if we look as the case where $v_0 = 0$, we get

$$
Z_{in} = -\frac{i}{ACs} \cot\left(\frac{\omega L}{s} \right)
$$

which is the usual expression for an transmission line open circuit stub, if we identify $Z_0 = \frac{1}{ACs}$.

5.2.2 Reflection Gain Device and Measurements

In an attempt to verify the voltage reflection gain Γ, we designed and fabricated a series of devices on the same GaAs/AlGaAs platform using the ultrahigh-mobility heterostructure wafers provided by Kenneth West and Loren Pfeiffer from Princeton University. We wish to replicate the situation described in the previous section as closely as possible, where we have the plasmon signal being reflected off an open circuit boundary, while the reflection coefficient is measured from the other. In the previous section, we calculated the reflection coefficient 5.2 and noticed that a key requirement for the voltage gain $|\Gamma| > 1$ is that Z_{BC} is as large as possible, i.e. the reflecting boundary is as close to an open circuit as possible. This may seem incongruent with the fact that one also needs to push a large current to enable large electron drift velocities so that the reflection coefficient is greater than 1. However, this situation is in fact achievable, because Z_{BC} is in general frequency dependent, and one can have a low load DC resistance, while having a large AC impedance. This function is exactly what microwave filters and bias tees provide, being able to selectively filter out certain frequencies and absorbing / reflecting others.

Therefore, the first step was to design a high-Q microwave filter with a large impedance at ~50 GHz and a low impedance at DC. The filter design I chose was based on quarter wave stubs, and designed and simulated using SONNET, a commercial microwave 2.5D simulation software. The filter design can be seen in Fig. 5.4. In this design, 4 symmetrical quarter wave open-circuit stubs cause the center of the filter to behave as a virtual AC

72

short. Thus, the ends of the filter appears as an AC open circuit. This particular design was chosen because of the extremely high Z_{BC} that it could achieve, due to the large quality factor of the quarter wave stubs. This design was fabricated and tested on blank GaAs wafers, and the performance was found to match the simulation very closely, with a $|Z_{BC}| > 4000\ \Omega$ at the resonance frequency of 42 GHz, which can be seen in Fig 5.4a. Furthermore, by placing it as close as possible to the 2DEG when using the filter for the gain measurement, one ensures that losses from any gold transmission lines are minimized.

The steps to fabricate a device to measure the gain was virtually identical to that of the devices used to measure the nonreciprocity. After designing the masks, the rectangular mesas to define the 2DEG boundaries were made, and Ni/Au/Ge contacts were deposited and annealed. Here, we required an additional etch step to remove the 1 μm GaAs/AlGaAs buffer layers underneath the active GaAs layers (which were grown to trap propagation of defects during the heterostructure growth process) and the gold transmission lines and microwave filters were deposited using e-beam evaporation and lifted off. The additional etch step was found to be necessary as the buffer layers were found to cause a significant loss in performance of the microwave filters.

Measurements of the fabricated circuits were made in the Lakeshore probe station with a network analyzer, with 2 Keithley 2400 source measure units (SMUs) providing DC biases for the each of the 2 ends of the 2DEG. The probe station was cooled to 10 K to increase the mobility of the 2DEG and the network analyzer calibrated using a the multi-line TRL calibration method [38]. In principle, the S-parameter measurements that the network analyzer reads are the reflection and transmission coefficients of the circuit, by accounting for losses in the biasing circuit, contacts, and 2DEG itself accurately, would
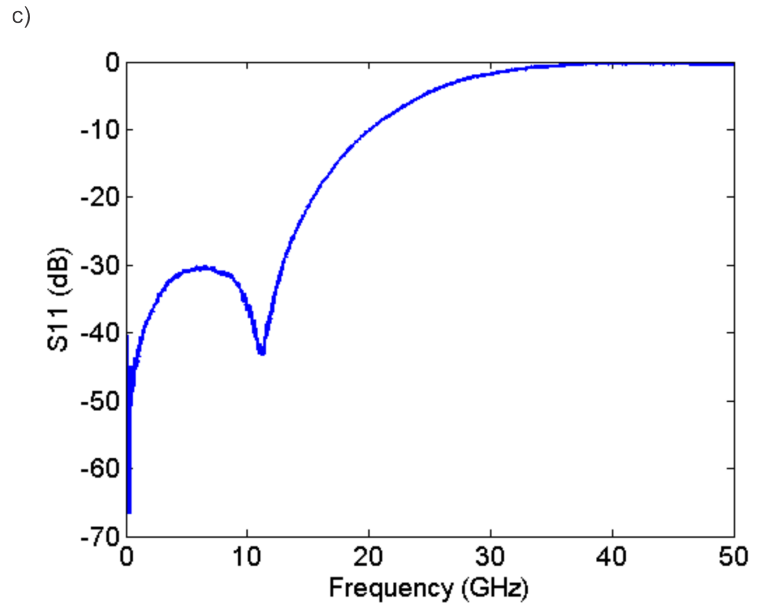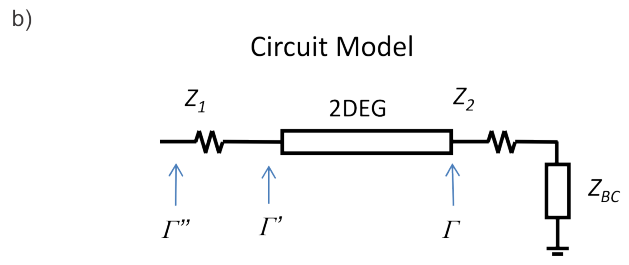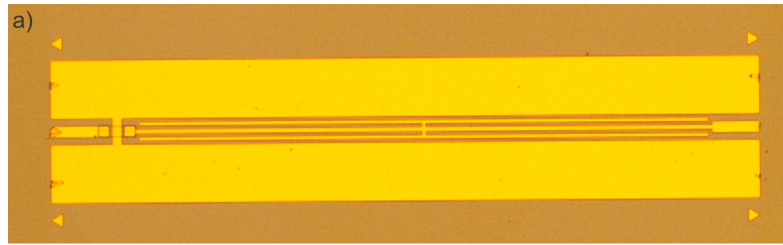
Figure 5.4: a) Figure showing graphene device designed to measure reflection gain. b) Circuit model for the device showing the contact impedances $Z_1 \approx R_1$ and $Z_2 \approx R_2$, which are largely resistive. c) Graph showing the performance of the microwave filter, which had a resonance frequency at 42 GHz. At resonance, the input impedance of the filter was $|Z_{BC}| > 4000 \ \Omega$.

translate to the reflection coefficients of the plasmons in the 2DEG. By changing the bias voltages to the 2DEG and applying a drift current, we aimed to directly measure these reflection coefficients.

Fig. 5.4b shows the simplest circuit model including the contact resistances and the parasitic pad capacitances. The challenge is that while we want to measure Γ, the reflection coefficient calculated in the previous subsection, we can only directly measure $\Gamma'' = S_{11}$, and thus some further analysis of the data is necessary to see the behaviour of Γ, and the analysis necessarily involves knowing the various circuit parameters in the model accurately. In general, the DC contact resistances we managed to achieve were on the order of $\sim 50\,\Omega$ for a $20\,\mu\mathrm{m} \times 20\,\mu\mathrm{m}$ contact, while we estimate the parasitic pad capacitances to be smaller than 0.1pF, which means that the bulk of the effect of the contact should be resistive and in practice the parasitic capacitance could be ignored. By fitting the measured S-parameters as a function of frequency to this circuit model, we could extract the 2DEG mobility (equivalently, plasmon scattering time τ), density n_0 and contact resistance parameters R_1 and R_2. This fit to determine the circuit model parameters was necessary because there was no independent way of obtaining the contact resistances, which could differ greatly from device to device. Using these parameter fits, one could extract the measured Γ' by using the known circuit model for the contact. The data from a representative device, DEV3, is shown in Fig. 5.5. Near the resonance point of 42GHz, as the magnitude of the current is increased, Γ' universally decreases as the magnitude of current I increases. However, depending on the direction of the current I, the decrease of the reflection coefficient Γ' was asymmetric with respect to the 0 current case: there was a smaller decrease in Γ' when the drift current flow direction was expected to show gain, $|\Gamma| > 1$ when $I > 0$

. These results suggest qualitatively that some voltage gain is indeed happening in the 2DEG system, manifesting itself as an asymmetric behaviour of the plasmonic response when it is subject to drift currents going into the filter, and out of the filter.

Unfortunately, the fits obtained did not allow us to extract the contact resistances accurately enough to obtain a clear measurement of the plasmon reflection gain Γ. The first problem is that loss from both the contact resistance R_1 and the plasmon scattering time τ lead to a similar outcome, namely a reduction in the absolute value of the measured S_{11} that was frequency independent. Thus, it was difficult for the model fit to separate these 2 effects, leading to a large uncertainty in the extracted model parameters R_1 and τ. Secondly, changing the bias to increase a current causes the mobility of the 2DEG to decrease, reducing the plasmon scattering time τ and lowering the measured reflected signal S_{11}, which further increases the uncertainty of the measurement. Further, it was unclear if we could rely on the assumption that R_1 remained constant as the bias current through the device increases. Lastly, the curve fitting to the S-parameter data were not always satisfactory with small R^2 values indicating poor fits to the circuit model, with the results somewhat dependent on choice of parameters to include in the circuit model (for example, R_2 is not expected to affect the results very strongly as it is in series with a very large impedance Z_{BC}, but in practice the results might depend on the form of R_2). This suggests that some degree of overfitting to the data may be occurring, even for the sample DEV3 whose results were shown in Fig. 5.5.
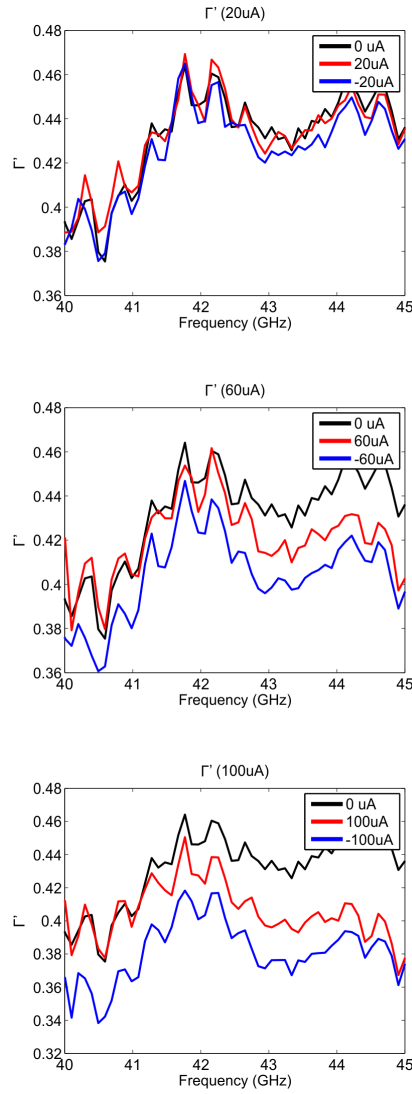
Figure 5.5: Graphs showing extracted Γ' from a representative sample (DEV3) for varying bias currents I. Each of the graphs shows the behaviour of Γ' as the I is changed from negative to positive. Near the resonance point of 42GHz, as the current is increased, Γ' decreases as the magnitude of current I increases, reflecting the decrease in mobility of the 2DEG, although the decrease is asymmetric with respect to $I = 0$.

5.3 Nonreciprocal plasmons in graphene

In this section, we will study the possibility of measuring similar nonreciprocal plasmons in graphene. Since it is also a 2D electron gas with a large L_K[28], its plasmons at microwave and THz frequencies can also be relatively slow ($\sim c/100$). While this may seem to be much larger than the velocities possible in the high mobility 2DEG described in the previous section, the advantage is that the high mobilities can persist even at room temperatures when the graphene is suspended or encapsulated by an ultraclean hBN surface. Thus, it should be possible to measure plasmons with quality factors $Q = \omega LK/R > 1$ at mm-wave frequencies, which would be much more difficult to achieve in a cryogenic environment.

5.3.1 Graphene Device Fabrication

In order to maximize this quality factor, we fabricated samples using exfoliated graphene and hBN crystals. The steps largely follow that of the fabrication of the GaAs/AlGaAs samples, although the recipes may differ completely. These crystals were stacked together using a dry transfer process (see AppendixA.3) and its edges etched to expose a small 1D surface to make ohmic contacts. The contact metal (Cr/Pd/Au) was deposited with e-beam evaporation, covering the exposed graphene edges and completing the contact. Part of the gate was also deposited at the same lithographic step, due to challenges aligning the write layers repeatably. Finally, the CPW lines, gate, and pads were deposited. An optical micrograph of the device is shown in Fig. 5.6a.
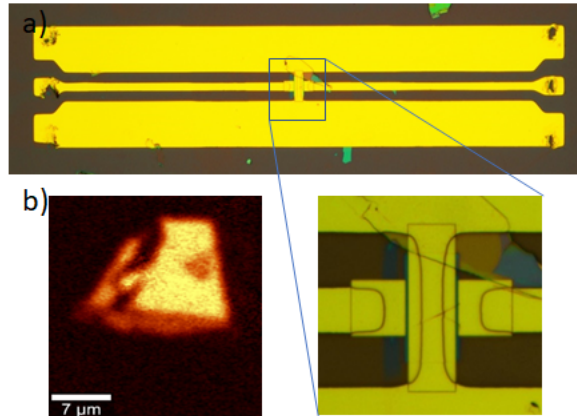
Figure 5.6: a) Optical Micrograph of the graphene device. b) Raman image of the graphene before patterning of the contacts and CPW lines. The non-ideal shape of the graphene is clearly visible as well as an air bubble trapped in the stack.

There are several key differences. The first was the much smaller active 2DEG area, only 7 μm by 5 μm , due to the size limitations of exfoliated samples. The second is the much longer coplanar waveguides, which extended 200μm away from the sample in each side. This was necessary to reduce cross-talk between the probe heads, which limited our first attempts at successful calibration. Lastly, we note that the graphene sample shown is not perfectly rectangular, but rather trapezoidal in shape, with an air bubble that is visible both optically and in the Raman image taken at the 2630 to 2730 cm^{-1} (Fig. 5.6b). These air bubbles were a common result of the stacking process, and may sometimes be mitigated by high-temperature annealing, but in this case it did not improve the sample.

5.3.2 Measurement and Analysis

Due to the mm-wave frequencies necessary to obtain a plasmon with $Q > 1$, we used Virginia Diode VNA extenders mounted on a Cascade Microtech PM8 probe station that

allow us to make vector network measurements of the graphene devices at up to 330GHz at room temperature. As in the case of GaAs/AlGaAs before, bias tees built-in to the waveguide probe heads were used to separate the mm-wave and DC excitation of the device, with 2 Keithley 2400s controlling the DC biases. Preliminary measurements of the graphene plasmon velocity have been made, demonstrating the gate dependence of the graphene plasmon velocity using methods similar to the previous section.

A graph of the measured plasmon velocity is shown in Fig. 5.7. From the measurement results, we see that at gate voltages within 1V of the dirac point, there is a large apparent divergence of the plasmon velocity. However, at these gate voltages, the graphene is very resistive and the transmission signal S_{21} is very small, so that the data is spurious and largely due to some parasitic transmission. Even if these points are disregarded, the measured plasmon velocities appear to follow a trend consistent with the theory with increasing plasmon velocity for increasing electron density. However, the values of the velocity appear to be off by a factor of 1.5. This could arise from a number of inaccuracies, mainly in the measurements of the graphene dimensions and hBN thicknesses.
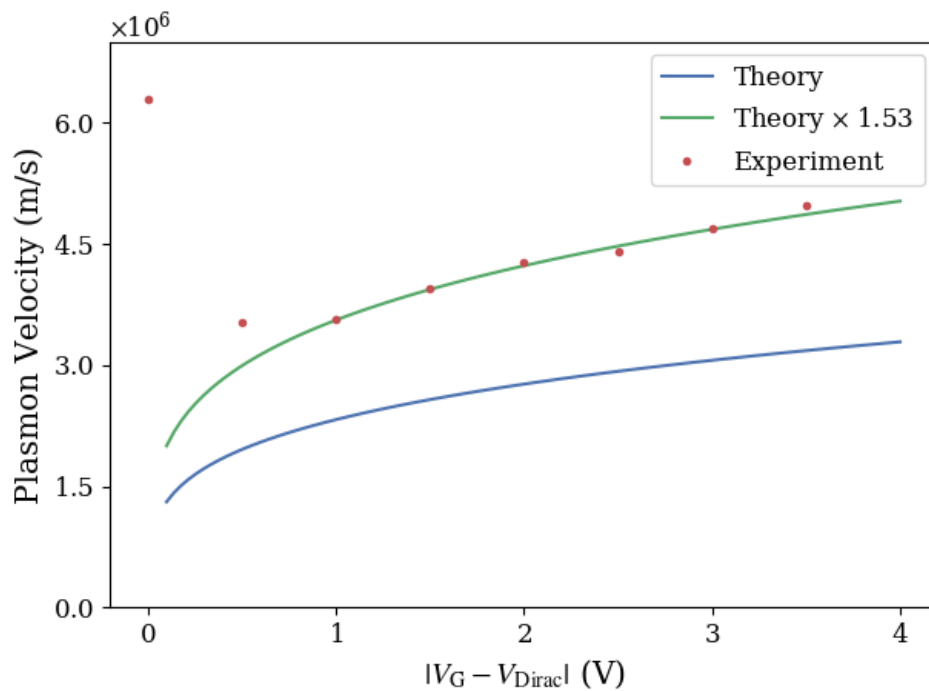
Figure 5.7: Measured plasmon velocity (red circles) vs the theory with no fit parameters (blue line). A better fit includes a factor of 1.53, which might account for possible deviations of the actual measurement device geometry from the idealized theory due to the non-ideal shape of the graphene.

Appendix A

Microfabrication Details and Recipes

This section documents the steps used in the fabrication of the samples, which were performed at the Center for Nanoscale Systems (CNS) cleanroom at Harvard University. Special credit for the initial development of these recipes goes Shannon Harvey and her co-workers in the Yacoby group for the fabrication of contacts on GaAs wafers, and many members of the Kim lab including Shi Jing, Laurel Anderson, Hiroshi Idzuchi and Carlos Forsythe for recipes involving the fabrication of graphene samples.

A.1   Lithography Processes

These were useful for both GaAs and Si wafers, although some dose testing was typically necessary due to process and tool variations. In particular, the size and shape of the wafer sections on which the samples were fabricated on has a surprisingly large influence on the thickness of the resist films due to variations in air flow around the wafer sections as it is

spin-coated. In this work, I used 8mm square GaAs wafer sections and 10mm square SiO_2 wafer sections.

A.1.1 S1805 single layer process

This is a general purpose resist recipe resulting in a film 480nm thick. This can be used to lift-off metal films up to ~100nm relatively easily (this is dependent on the size of the features).

1. Spin-coat S1805 at 4000 RPM

2. 60 s soft-bake on a hotplate at 115 °C. This should result in a film ~480nm

3. Expose using the Heidelberg Maskless Aligner, or MLA (Dose: 70 mJ/cm^2 with 405 nm laser)

4. Develop in CD-26 60s

5. Rinse with deionized water

6. 60s hard-bake 115 °C

Alternatively, if writing using a hard mask, MJB4 mask aligner can be used (Dose: 3 seconds at 15 mW lamp power) with a 9 second develop in MF319. If the resist is to be used as a mask for a wet etch, one can consider a longer hard-bake e.g. 10 min at 100 °C .

A.1.2 AZ5214E Image Reversal process

This is used to obtain a lithographic pattern with a slight undercut, to enable deposition of metal films up to ~400nm thick. This recipe and undercut is usually fairly consistent, and allows for liftoff in acetone to be complete in half an hour.

1. Spin-coat S1805 at 4000 RPM

2. 60 s soft-bake on a hotplate at 100 °C.

3. Expose on either the MLA (Dose: 25 mJ/cm^2 with 405 nm laser)

4. 60 s reversal bake on a hotplate at 120 °C.

5. Flood exposure 45 seconds on the MJB4.

6. Develop in AZ726 MIF developer for 25 s.

7. Rinse with deionized water

Alternatively, one can expose with the MJB4 (Dose 0.4 s at 15.1 mW lamp power)

A.1.3 E-beam PMMA single layer process

This is a general purpose resist recipe resulting in a film 400nm thick. This can also be used for liftoff of <100nm films and the pattern edges are relatively clean and ear-free for ~5-10 μm features.

1. Spin-coat PMMA 950K C4 at 4000RPM

2. Bake at 180 °C for 60 s.

3. Expose on Elionix F125 125 keV e-beam writer, dose 1800 μC/cm^2 at 1nA, usually using 500 μm field size and 200 000 dots.

4. Develop 30s in MIBK:IPA 1:3

5. Rinse off with IPA

A.1.4   E-beam PMMA/MMA Bilayer process

This is used to obtain a lithographic pattern with a large undercut to allow deposition of thicker metal films. Unfortunately the amount of undercut is difficult to control and very highly dependent on the development time, and so is not suitable for very fine (<2 μm) patterns.

1. Spin-coat MMA (8.5) MMA at 4000RPM

2. Bake at 150 °C for 90 s.

3. Spin-coat PMMA 950K C4 at 4000RPM

4. Bake at 180 °C for 90 s.

5. Expose on Elionix F125 125 keV e-beam writer, dose 1800 μC/cm^2 at 5nA, usually using 500 μm field size and 50 000 dots.

6. Develop 20s in MIBK:IPA 1:3

7. Rinse off with IPA

A.2 GaAs-specific Recipes

A.2.1 Mesa Etching

S1805 spun at 4000 RPM was used as an etch mask to define GaAs mesas. The GaAs was etched in a well mixed dilute acid mixture H_3PO_4:H_2O_2:H_2O 1 : 1 : 25 which has an etch rate of ~2000 Å/min. The GaAs samples I received from Kenneth West had the active layer 80 nm under the surface, so an etch for 30 seconds is usually enough to etch past the unmasked AlGaAs/GaAs layers. This etch rate was not very constant (probably due to different AlGaAs and GaAs etch rates) and so should be checked with a profilometer.

A.2.2 Contact formation

After mesas were etched, n-type contacts to the GaAs/AlGaAs electron gas were defined by photolithography by using AZ5214E. The surface was de-scummed and cleaned with the barrel plasma asher (30 sccm O_2, 100W, 1 minute). This was followed by a quick 15 s dip in a 1:1 HCl : H_2O solution to remove any surface oxide, rinsed in dionized water, blow dried with N_2 and immediately put into an evaporator. The evaporator should be loaded with materials and prepared earlier to minimize the time exposed to atmosphere after the oxide removal step, as the surface oxide formation happens within minutes on contact with O_2 in the air. Ni/Au/Ge/Ni/Au with thickesses of 6 nm / 30 nm / 60nm / 20nm / 150 nm was thermally evaporated in as low a pressure as possible. I took note to use a new boat for Ni evaporation for every run, as melted Ni is chemically reacts with the tungsten boats, making them brittle and a very high chance of cracking in subsequent runs.

After liftoff in acetone for half an hour, rinsing and blow-drying with isopropyl alcohol (IPA), the contacts were annealed in a rapid thermal annealer for 20s at 460 °C in a forming gas atmosphere. This should result in contact metal surface taking on a mottled appearance, as the Au/Ge eutectic melts and forms spikes into into the GaAs.[]

A.3   hBN-Graphene-specific recipes

A.3.1   Exfoliation

Graphene and hBN crystals were mechanically exfoliated onto 280nm SiO_2 wafers. An optical resonance allows suitable flakes of crystals to be easily identified by eye using an optical microscope and characterized, most often using a Veeco AFM to check a clean flat surface on the hBN and a WITec Raman confocal microscope to check that the graphene was single layer.

A.3.2   Crystal Stacking

After the appropriate hBN and graphene flakes were identified, they were stacked using a dry-transfer method using a modified probe station. A small 4 mm × 4 mm PDMS stamp (1 mm thick) was placed onto a glass slide, and heated to 180 °C for it to adhere to the transparent glass slide. A thin film of PC polymer (2mm × 2mm) was placed onto the PDMS stamp and the stack held in place with a micropositioner. With the aid of the probe station microscope looking through the glass slide / PDMS / PC, the PC was put into contact with the wafer section near a clean hBN flake. Then, the wafer substrate was slowly heated to 80°C, causing it expand pushing it into the PC and PDMS and causing

the flake to be slowly engulfed by the PC. The higher temperature also causes the PC to be more sticky, and the micropositioner can then be raise to lift off the flake from the substrate surface.

The aforementioned process can then be repeated with subsequent flakes on the same PC piece, with the different crystals stacked on top of each other since one can use the microscope to align the crystals as they come into contact. In fact, after initial pickup of the first hBN crystal, subsequent crystals are more easily picked up due to the strong Van der Waals forces between hBN and graphene.

After successfully stacking the hBN and graphene crystals, the whole stack was put into contact with a fresh new substrate (in this work, we used High-Resistivity Float Zone (HRFZ) silicon with 280nm of oxide, which was necessary to reduce mm-wave substrate losses). The substrate was heated to 140°C , causing the PC to undergo a plastic transition, releasing it from the PDMS and leaving it behind on the fresh substrate. The PC was then dissolved in Chloroform for 5 min, rinsed with isopropyl alcohol and blow dried. Lastly, the stack was annealed in a vacuum at 350°C for 1 hour. This reduces the number of bubbles and defects in the stack.

A.3.3   Graphene Edge Contacts

Electrical contact to the graphene was made using 1D edge contacts[39]. Electron beam lithography (See A.1.3) was used to define an etch mask, and the hBN-graphene-hBN stack was dry-etched to expose edges of the graphene. The dry etching was performed in a Surface Technology Systems Inductively Coupled Plasma etch system, with 10 sccm CHF_3, 5 sccm Ar and 2 sccm O_2. The exposed wafer was immediately placed into an

evaporator, and 2nm Cr / 10nm Pd / 80nm Au was deposited at about a 30° angle to cover the exposed graphene sidewall edge.

Appendix B

Applications of Group Theory to Plasmonic Crystals

This section will provide an overview to of how group theory applies to symmetries of electromagnetic waves. In particular, we wish to answer these questions:

1. What does it mean to classify solutions to the electromagnetic wave equations according to irreducible representations of a symmetry group?

2. What restrictions on the coupling coefficients does group theory predict?

B.1   Key concepts and definitions

A representation, $\mathscr{R}_{\mathscr{G}}$, of a group, $\mathscr{G}$, is a group of square matrices $\mathbf{D}(A)$ that is homomorphic to the abstract group $\mathscr{G}$. Homomorphic means that the mapping preserves the algebraic structure. Stated more simply, each element of $\mathscr{G}$ (let's call them A) has a

corresponding square matrix $\mathbf{D}(A)$ such that $\mathbf{D}(A)\mathbf{D}(B) = \mathbf{D}(AB)$. A trivial representation is the matrix $\mathbf{D}(A) = (1)$, which is obviously true for any symmetry group $\mathscr{G}$.

Representations are not unique! Firstly, we note that the trivial representation is always a possible representation. Example: given a representation $\mathscr{R}_\mathscr{G}$ whose elements are $\mathbf{D}(A)$, a 'similarity transformation' $\mathbf{U}\mathbf{D}(A)\mathbf{U}^{-1}$ results in another set $\mathscr{R}'_\mathscr{G}$ that is also a representation.

Even the dimension of D is not unique. Given two representations $\mathscr{R}_\mathscr{G}$ and $\mathscr{R}'_\mathscr{G}$ with elements $\mathbf{D}(A)$ and $\mathbf{D}'(A)$ respectively, we can generate another representation using the matrices

$$\begin{pmatrix} \mathbf{D}(A) & \mathbf{0} \\ \mathbf{0} & \mathbf{D}'(A) \end{pmatrix}$$

This matrix is 'block-diagonal', i.e. it has submatrices on the diagonal in blocks.

The concept of a representation's irreducibility is overcomes this non-uniqueness. Definition: if one can use a similarity transformation to put a representation's matrices into block-diagonal form, then the representation is reducible. Otherwise, it is irreducible, which means that it cannot be expressed in terms of representations with lower dimensionality.

B.2 Application to the wave equation

The wave equation we want to solve to obtain the is is the stationary time-harmonic electric fields is the wave equation

$$\nabla \times (\nabla \times \mathbf{E}) = k_0^2 \mu_0 \left(\varepsilon_r - \frac{j\sigma}{\omega\varepsilon_0} \right) \mathbf{E}$$

This is basically an eigenvalue equation in $\mathbf{E}(\mathbf{r})$, ignoring some nonlinearity introduced by the frequency dependent conductivity.

$$\mathscr{F}(\mathbf{E}(\mathbf{r})) = \omega^2 \mathbf{E}(\mathbf{r})$$

$\mathscr{F}$ encodes all the information about the structure and excitations of our system. If there is symmetry in $\mathscr{F}$, we may write

$$\left[\mathscr{F}, \hat{P}_R\right] = 0$$

where the $\hat{P}_R$ form a symmetry group. Since the system is invariant under the action of $\hat{P}_R$, the eigenfunctions cannot be changed under the operation of $\hat{P}_R$. If $\mathscr{F}(\mathbf{E}_n(\mathbf{r})) = \omega_n^2 \mathbf{E}_n(\mathbf{r})$ is a solution, then

$$\mathscr{F}\left(\hat{P}_R \mathbf{E}_n(\mathbf{r})\right) = \omega_n^2 \hat{P}_R \mathbf{E}_n(\mathbf{r})$$

In other words, $\hat{P}_R \mathbf{E}_n(\mathbf{r})$ is an equally valid solution with the SAME eigenvalue ω_n^2.

What happens for degeneracies? Suppose n is a k-fold degenerate level. Then any linear combination of $\mathbf{E}_{n1}(\mathbf{r})$ to $\mathbf{E}_{nk}(\mathbf{r})$ is a solution to the wave equation (this is the basis

for the representation). We claim that applying the symmetry operation gives

$$\hat{P}_R \mathbf{E}_{n\alpha}(\mathbf{r}) = \sum_j \mathbf{E}_{nj}(\mathbf{r}) \times \left[D^{(n)}(R) \right]_{j\alpha}$$

where $\left[D^{(n)}(R) \right]_{j\alpha}$ are elements of the irreducible representation of the group of $\hat{P}_R$, i.e. $\mathscr{R}$. The outline of the proof is to consider the action of

$$\hat{P}_R \hat{P}_S \mathbf{E}_{n\alpha}(\mathbf{r}) = \sum_k \mathbf{E}_{nk}(\mathbf{r}) \left[D^{(n)}(R) D^{(n)}(S) \right]_{j\alpha}$$

which is equal to $\hat{P}_{RS} \mathbf{E}_{n\alpha}(\mathbf{r}) = \sum_j \mathbf{E}_{nj}(\mathbf{r}) \times \left[D^{(n)}(RS) \right]_{j\alpha}$.

The dimension of the irreducible representation $\dim(\mathbf{D})$ is equal to the degeneracy of the eigenvalue ω_n^2.

B.3   Classification of eigenmodes

The reasoning is as follows:

1. The symmetry operations $\hat{P}_R$ commute with the operator $\mathscr{F}$.

2. These symmetry operations form an abstract symmetry group, $\mathscr{G}$ with elements R.

3. If $\mathbf{E}_n$ is an eigenfunction with eigenvalue ω_n^2 then $\hat{P}_R \mathbf{E}_n$ is also an eigenfunction with the same eigenvalue. If ω_n^2 is k-fold degenerate,

$$\hat{P}_R \mathbf{E}_{n\alpha}(\mathbf{r}) = \sum_j \mathbf{E}_{nj}(\mathbf{r}) \times \left[D^{(n)}(R) \right]_{j\alpha}$$

4. It can be shown that the $\left[D^{(n)}(R)\right]_{j\alpha}$ is itself a group representation of $\mathscr{G}$. There are several irreducible representations of $\mathscr{G}$, so every $\mathbf{E}_n(\mathbf{r})$ must correspond to one of these.

B.4 Application to graphene plasmonic crystals

Our graphene plasmonic crystals are hexagonal and therefore have the C_{6v} point group symmetry, meaning that they have a 6-fold rotation axis and 6 mirror planes. According to group theory[13], the eigenfunctions (which are the stationary solutions to the 3D electromagnetic wave equations in a region with C_{6v} symmetry) can be classified into an irreducible representation of this group. In other words, each of the eigensolutions that we find from the finite element method, $E_{p,z}(\mathbf{r})$, where $\mathbf{r}$ is the real-space coordinate, must be classified into one of the 6 irreducible representations of the C_{6v} group which we call A_1, A_2, B_1, B_2, E_1, E_2, following typical crystallographic conventions . Furthermore, the action of each of the group elements, R (such as rotations or reflections), on one of these solutions must return an electric field distribution that is itself a solution to the wave equation.

For example, consider the electromagnetic modes of GPC1, with $a = 3 \ \mu$m and $D = 2 \ \mu$m (Fig. 2a, 2c of main text). The fourth band crosses the Γ point at 5.7 THz, i.e. there is an eigensolution at that frequency. If we denote rotation by $60°$ as R_{C_6}, we find that $R_{C_6}(E_{p,z}(\mathbf{r})) = -E_{p,z}(\mathbf{r})$, and reflection along the y-axis has the following relationship $R_{\sigma_y}(E_{p,z}(\mathbf{r})) = E_{p,z}(\mathbf{r})$. These are both possible solutions to the wave equation. For non-degenerate modes, the coefficient in front of the right hand side tells us the character, $\chi_\phi(R)$, of the representation, ϕ. By examining the known character table for the C_{6v} group
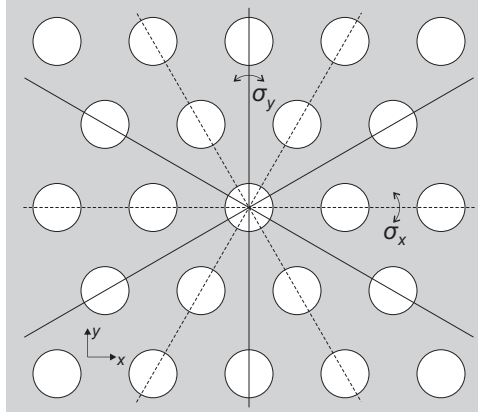
Figure B.1: Figure showing the reflection axes of the hexagonal lattice.

(Table S1), the only representation that responds to the symmetry operations in this way is B_1, and so the mode at 5.7 THz is a B_1 mode.

C_{6v}	E	$2C_6$	$2C_3$	C_2	$3\sigma_y$	$3\sigma_x$
A_1	1	1	1	1	1	1
A_2	1	1	1	1	-1	-1
B_1	1	-1	1	-1	1	-1
B_2	1	-1	1	-1	-1	-1
E_1	2	1	-1	-2	0	0
E_2	2	-1	-1	2	0	0

Table B.1: **Character Table for the C_{6v} group.** The entries are values of the character, $\chi_\phi(R)$, of symmetry transformations, R (columns), when they act on the irreducible representations, ϕ (rows).

This identification can also be extended to doubly degenerate modes. As before, we examine how the electric field changes under a transformation R, i.e.

$$R \begin{pmatrix} E_{p,1,z}(\mathbf{r}) \\ E_{p,2,z}(\mathbf{r}) \end{pmatrix} = \mathbf{A} \begin{pmatrix} E_{p,1,z}(\mathbf{r}) \\ E_{p,2,z}(\mathbf{r}) \end{pmatrix}$$

where $E_{p,1,z}(\mathbf{r})$ and $E_{p,1,z}(\mathbf{r})$ are the 2 degenerate eigensolutions. The character is defined to be $\chi_\phi(R) = \text{Tr}(\mathbf{A})$. Identifying the character under each of the transformations allows us to classify each of the electromagnetic modes found by the finite element method solver at the Γ point into the right representation (Table S2).

Furthermore, electromagnetic waves propagating in free space are also solutions of the wave equation, and so we must be able to classify it as one of the irreducible representations of the C_{6v} point group in exactly the same manner as above. Firstly, it is doubly degenerate due to the two polarizations, and secondly, $180°$ rotations (C_2) flip the sign of the fields,

$$R \begin{pmatrix} E_{1,z}(\mathbf{r}) \\ E_{2,z}(\mathbf{r}) \end{pmatrix} = - \begin{pmatrix} E_{1,z}(\mathbf{r}) \\ E_{2,z}(\mathbf{r}) \end{pmatrix}$$

which means that the character is $\chi_\phi(R_{C_2}) = -2$. Using the character table, we conclude that free space radiation propagating in the z- direction has the E_1 representation.

With this machinery we can now fully appreciate why certain electromagnetic modes do not couple to the free-space radiation, even when the in-plane wave vectors are conserved. Spatial symmetry requirements demand that the electromagnetic modes for both the graphene plasmonic crystals and free space respond in the same way under the action of the symmetry operations, and so only E_1 modes of the graphene plasmonic crystals can couple to free space, which for this particular graphene plasmonic crystal are modes 5, 6, 10 and 11.

Mode Number	2	3	4	5	6	7	8	9	10	11
Irreducible Representation	E_2	E_2	B_1	E_1	E_1	B_2	E_2	E_2	E_1	E_1

Table B.2: **Classification of the electromagnetic modes of the GPC1 with** $a = 3\,\mu\text{m}$ **and** $D = 2\,\mu\text{m}$**.** Only the modes 5, 6, 10 and 11 have the same irreducible representation as free-space radiation and can couple to it.

Appendix C

Quantum Capacitance of 1D Electrons

Consider N free electrons in a 1D box of length L. The total energy of electrons is given by

$$
\begin{aligned}
E &= \sum_{|k|<k_F} \frac{\hbar^2 k^2}{2m} \\
&= \frac{L}{2\pi} \int_{-k_F}^{k_F} \frac{\hbar^2 k^2}{2m} dk \\
&= \frac{\hbar^2 k_F^3 L}{6\pi m} \\
&= \frac{\hbar^2 \pi^2 N^3}{6mL^2}
\end{aligned}
$$

Now consider a 1D box of length $2L$ divided by a wall into two parts with N free electrons in each part. If we displace the wall from the middle point of the box by some distance x, the total energy is

$$
E(x) = \frac{\hbar^2 \pi^2 N^3}{6m} \left(\frac{1}{(L+x)^2} + \frac{1}{(L-x)^2} \right)
$$

The force corresponding to this energy term is

$$
\begin{aligned}
F = -\frac{\partial E}{\partial x} &= \frac{\hbar^2 \pi^2 N^3}{3m} \left(\frac{1}{(L+x)^3} - \frac{1}{(L-x)^3} \right) \\
&= \frac{\hbar^2 \pi^2 N^3}{3mL^3} \left(-\frac{6x}{L} \right) \\
&= -\frac{2\pi^2 \hbar^2 N^3}{mL^4} x
\end{aligned}
$$

Now if we wish to model this system by a quantum capacitance per unit length c_q, we would have an energy term

$$
E(x) = \frac{N^2 e^2}{2c_q} \left(\frac{1}{L+x} + \frac{1}{L-x} \right)
$$

which leads to a restoring force

$$
\begin{aligned}
F(x) &= \frac{N^2 e^2}{2c_q} \left(\frac{1}{(L+x)^2} - \frac{1}{(L-x)^2} \right) \\
&= \frac{N^2 e^2}{2c_q L^2} \left(-4\frac{x}{L} \right) \\
&= -\frac{2N^2 e^2}{c_q L^3} x
\end{aligned}
$$

Comparing coefficients of the restoring force, we obtain

$$
c_q = \frac{e^2 mL}{\hbar^2 \pi^2 N}
$$

Now, what if the system also has an electrostatic capacitance c_{es} per unit length? Then the total energy is given by

$$
\begin{aligned}
E(x) &= \frac{\hbar^2 \pi^2 N^3}{6m} \left(\frac{1}{(L+x)^2} + \frac{1}{(L-x)^2} \right) + \frac{N^2 e^2}{2c_{es}} \left(\frac{1}{L+x} + \frac{1}{L-x} \right) \\
F(x) &= -\frac{2\pi^2 \hbar^2 N^3}{mL^4} x - \frac{2N^2 e^2}{c_{es}L^3} x \\
&= -\frac{2N^2 e^2}{c_q L^3} x - \frac{2N^2 e^2}{c_{es}L^3} x \\
&= -\frac{2N^2 e^2}{L^3} \left(\frac{1}{c_q} + \frac{1}{c_{es}} \right) x
\end{aligned}
$$

Thus the corresponding total capacitance is $\frac{1}{c_{eff}} = \frac{1}{c_q} + \frac{1}{c_{es}}$. This calculation shows that the quantum capacitance is in series with the electromagnetic capacitance, which means that the smaller of the capacitances dominate. In most normal materials, c_q is large enough that c_{es} is entirely dominant. However, in 2D materials, the quantum capacitance can be made small enough due to the small density of states that its effects can be measured.

Bibliography

[1] Neil W. Ashcroft and N. David Mermin. *Solid State Physics*. Cengage Learning, New York, 1 edition edition, January 1976.

[2] Kitty Y. M. Yeung, Jingyee Chee, Hosang Yoon, Yi Song, Jing Kong, and Donhee Ham. Far-infrared graphene plasmonic crystals for plasmonic band engineering. *Nano Letters*, 14(5):2479–2484, 2014. PMID: 24678885.

[3] Jingyee Chee, Hosang Yoon, Ling Qin, and Donhee Ham. Plasmonic mass and johnson-nyquist noise. *Nanotechnology*, 26(35):354002, 2015.

[4] Xuesong Li, Weiwei Cai, Jinho An, Seyoung Kim, Junghyo Nah, Dongxing Yang, Richard Piner, Aruna Velamakanni, Inhwa Jung, Emanuel Tutuc, Sanjay K. Banerjee, Luigi Colombo, and Rodney S. Ruoff. Large-Area Synthesis of High-Quality and Uniform Graphene Films on Copper Foils. *Science*, 324(5932):1312–1314, June 2009.

[5] Alfonso Reina, Xiaoting Jia, John Ho, Daniel Nezich, Hyungbin Son, Vladimir Bulovic, Mildred S. Dresselhaus, and Jing Kong. Large area, few-layer graphene

films on arbitrary substrates by chemical vapor deposition. *Nano Letters*, 9(1):30–35, 2009. PMID: 19046078.

[6] L. M. Malard, M. A. Pimenta, G. Dresselhaus, and M. S. Dresselhaus. Raman spectroscopy in graphene. *Physics Reports*, 473(5):51–87, April 2009.

[7] Eduardo J. H. Lee, Kannan Balasubramanian, Ralf Thomas Weitz, Marko Burghard, and Klaus Kern. Contact and edge effects in graphene devices. *Nature Nanotechnology*, 3:486 EP –, Jun 2008.

[8] A. N. Grigorenko, M. Polini, and K. S. Novoselov. Graphene plasmonics. *Nature Photonics*, 6(11):749–758, November 2012.

[9] A. Yu. Nikitin, F. Guinea, and L. Martin-Moreno. Resonant plasmonic effects in periodic graphene antidot arrays. *Applied Physics Letters*, 101(15):151119, October 2012.

[10] Yu. V. Bludov, Aires Ferreira, N. M. R. Peres, and M. I. Vasilevskiy. A primer on surface plasmon-polaritons in graphene. *International Journal of Modern Physics B*, 27(10):1341001, April 2013.

[11] Long Ju, Baisong Geng, Jason Horng, Caglar Girit, Michael Martin, Zhao Hao, Hans A. Bechtel, Xiaogan Liang, Alex Zettl, Y. Ron Shen, and Feng Wang. Graphene plasmonics for tunable terahertz metamaterials. *Nature Nanotechnology*, 6(10):630–634, October 2011.

[12] Onur Kilic, Michel Digonnet, Gordon Kino, and Olav Solgaard. Controlling uncoupled resonances in photonic crystals through breaking the mirror symmetry. *Optics Express*, 16(17):13090–13103, August 2008.

[13] Kazuaki Sakoda. *Optical Properties of Photonic Crystals*. Springer, 2005.

[14] Oskar Painter and Kartik Srinivasan. Localized defect states in two-dimensional photonic crystal slab waveguides: A simple model based upon symmetry analysis. *Phys. Rev. B*, 68:035110, Jul 2003.

[15] Xiaolong Zhu, Weihua Wang, Wei Yan, Martin B. Larsen, Peter Bøggild, Thomas Garm Pedersen, Sanshui Xiao, Jian Zi, and N. Asger Mortensen. Plasmon-phonon coupling in large-area graphene dot and antidot arrays fabricated by nanosphere lithography. *Nano Letters*, May 2014.

[16] Shanhui Fan and J. D. Joannopoulos. Analysis of guided resonances in photonic crystal slabs. *Physical Review B*, 65(23):235112, June 2002.

[17] Kitty Y. M. Yeung, Hosang Yoon, William Andress, Ken West, Loren Pfeiffer, and Donhee Ham. Two-path solid-state interferometry using ultra-subwavelength two-dimensional plasmonic waves. *Applied Physics Letters*, 102(2):021104, January 2013.

[18] William F. Andress, Hosang Yoon, Kitty Y. M. Yeung, Ling Qin, Ken West, Loren Pfeiffer, and Donhee Ham. Ultra-Subwavelength Two-Dimensional Plasmonic Circuits. *Nano Letters*, 12(5):2272–2277, May 2012.

[19] Hugen Yan, Xuesong Li, Bhupesh Chandra, George Tulevski, Yanqing Wu, Marcus Freitag, Wenjuan Zhu, Phaedon Avouris, and Fengnian Xia. Tunable infrared plasmonic devices using graphene/insulator stacks. *Nature Nanotechnology*, 7(5):330–334, May 2012.

[20] Chi-Fan Chen, Cheol-Hwan Park, Bryan W. Boudouris, Jason Horng, Baisong Geng, Caglar Girit, Alex Zettl, Michael F. Crommie, Rachel A. Segalman, Steven G. Louie, and Feng Wang. Controlling inelastic light scattering quantum pathways in graphene. *Nature*, 471(7340):nature09866, March 2011.

[21] J. B. Johnson. Thermal agitation of electricity in conductors. *Phys. Rev.*, 32:97–109, Jul 1928.

[22] H. Nyquist. Thermal agitation of electric charge in conductors. *Physical Review*, 32(1):110–113, July 1928.

[23] R. Kubo. The fluctuation-dissipation theorem. *Reports on Progress in Physics*, 29(1):255, January 1966.

[24] Herbert Callen and Theodore Welton. Irreversibility and generalized noise. *Physical Review*, 83(1):34–40, July 1951.

[25] Jorge R. Zurita-Sánchez and Carsten Henkel. Lossy electrical transmission lines: Thermal fluctuations and quantization. *Phys. Rev. A*, 73:063825, Jun 2006.

[26] Hosang Yoon, Kitty Y. M. Yeung, Philip Kim, and Donhee Ham. Plasmonics with two-dimensional conductors. *Philosophical Transactions of the Royal Society of London A: Mathematical, Physical and Engineering Sciences*, 372(2012), 2014.

[27] H. Ehrenreich and M. H. Cohen. Self-consistent field approach to the many-electron problem. *Phys. Rev.*, 115:786–790, Aug 1959.

[28] Hosang Yoon, Carlos Forsythe, Lei Wang, Nikolaos Tombros, Kenji Watanabe, Takashi Taniguchi, James Hone, Philip Kim, and Donhee Ham. Measurement of collective dynamical mass of dirac fermions in graphene. *Nature Nanotechnology*, 9(8):594–599, August 2014.

[29] C. R. Dean, A. F. Young, I. Meric, C. Lee, L. Wang, S. Sorgenfrei, K. Watanabe, T. Taniguchi, P. Kim, K. L. Shepard, and J. Hone. Boron nitride substrates for high-quality graphene electronics. *Nature Nanotechnology*, 5(10):722–726, 2010.

[30] Saeed H. Abedinpour, G. Vignale, A. Principi, Marco Polini, Wang-Kong Tse, and A. H. MacDonald. Drude weight, plasmon dispersion, and ac conductivity in doped graphene sheets. *Physical Review B*, 84(4):045429, July 2011.

[31] Hugen Yan, Fengnian Xia, Zhiqiang Li, and Phaedon Avouris. Plasmonics of coupled graphene micro-structures. *New Journal of Physics*, 14(12):125001, December 2012.

[32] Hosang Yoon, Kitty Y. M. Yeung, Vladimir Umansky, and Donhee Ham. A Newtonian approach to extraordinarily strong negative refraction. *Nature*, 488(7409):65–69, August 2012.

[33] V. Ariel and A. Natan. Electron effective mass in graphene. In *2013 International Conference on Electromagnetics in Advanced Applications (ICEAA)*, pages 696–698, September 2013.

[34] K. S. Novoselov, A. K. Geim, S. V. Morozov, D. Jiang, M. I. Katsnelson, I. V. Grigorieva, S. V. Dubonos, and A. A. Firsov. Two-dimensional gas of massless dirac fermions in graphene. *Nature*, 438(7065):197–200, November 2005.

[35] Yuanbo Zhang, Yan-Wen Tan, Horst L. Stormer, and Philip Kim. Experimental observation of the quantum hall effect and berry's phase in graphene. *Nature*, 438(7065):201–204, November 2005.

[36] Michael Dyakonov and Michael Shur. Shallow water analogy for a ballistic field effect transistor: New mechanism of plasma wave generation by dc current. *Phys. Rev. Lett.*, 71:2465–2468, Oct 1993.

[37] L. C. Ó Súilleabháin, H. P. Hughes, A. C. Churchill, D. A. Ritchie, M. P. Grimshaw, and G. A. C. Jones. Raman studies of plasmon modes in a drifting two-dimensional electron gas. *Journal of Applied Physics*, 76(3):1701–1705, 1994.

[38] R. B. Marks. A multiline method of network analyzer calibration. *IEEE Transactions on Microwave Theory and Techniques*, 39(7):1205–1215, Jul 1991.

[39] L. Wang, I. Meric, P. Y. Huang, Q. Gao, Y. Gao, H. Tran, T. Taniguchi, K. Watanabe, L. M. Campos, D. A. Muller, J. Guo, P. Kim, J. Hone, K. L. Shepard, and C. R. Dean. One-dimensional electrical contact to a two-dimensional material. *Science*, 342(6158):614–617, 2013.